AGU PUBLICATIONS

JGR

Journal of Geophysical Research: Atmospheres

RESEARCH ARTICLE

10.1002/2015JD023848

Key Points:
- TCAP provides a data set to investigate science questions and evaluate model performance
- There is a large amount of variability in aerosol properties near northeast coast of North America
- Aerosol layers aloft have a large impact on aerosol optical depth

Supporting Information:
- Figures S1 and S2 and Captions for Tables S1–S3
- Table S1
- Table S2
- Table S3

Correspondence to:
L. K. Berg,
Larry.Berg@pnnl.gov

Citation:
Berg, L. K., et al. (2016), The Two-Column Aerosol Project: Phase I—Overview and impact of elevated aerosol layers on aerosol optical depth, *J. Geophys. Res. Atmos.*, *121*, 336–361, doi:10.1002/2015JD023848.

Received 25 JUN 2015
Accepted 30 NOV 2015
Accepted article online 2 DEC 2015
Published online 8 JAN 2016

The Two-Column Aerosol Project: Phase I—Overview and impact of elevated aerosol layers on aerosol optical depth

Larry K. Berg[1], Jerome D. Fast[1], James C. Barnard[2], Sharon P. Burton[3], Brian Cairns[4], Duli Chand[1], Jennifer M. Comstock[1], Stephen Dunagan[5], Richard A. Ferrare[3], Connor J. Flynn[1], Johnathan W. Hair[3], Chris A. Hostetler[3], John Hubbe[1], Anne Jefferson[6,7], Roy Johnson[5], Evgueni I. Kassianov[1], Celine D. Kluzek[1], Pavlos Kollias[8], Katia Lamer[8], Kathleen Lantz[7], Fan Mei[1,9], Mark A. Miller[10], Joseph Michalsky[6], Ivan Ortega[7,11], Mikhail Pekour[1], Ray R. Rogers[3], Philip B. Russell[5], Jens Redemann[5], Arthur J. Sedlacek III[9], Michal Segal-Rosenheimer[12], Beat Schmid[1], John E. Shilling[1], Yohei Shinozuka[12], Stephen R. Springston[9], Jason M. Tomlinson[1], Megan Tyrrell[13], Jacqueline M. Wilson[1], Rainer Volkamer[7,11], Alla Zelenyuk[1], and Carl M. Berkowitz[1]

[1]Pacific Northwest National Laboratory, Richland, Washington, USA, [2]University of Nevada, Reno, Reno, Nevada, USA, [3]NASA Langley Research Center, Hampton, Virginia, USA, [4]NASA Goddard Institute for Space Studies, New York, New York, USA, [5]NASA Ames Research Center, Moffett Field, California, USA, [6]NOAA Earth System Research Laboratory, Boulder, Colorado, USA, [7]Cooperative Institute for Research in Environmental Sciences, University of Colorado Boulder, Boulder, Colorado, USA, [8]Department of Atmospheric and Oceanic Sciences McGill University, Montreal, Quebec, Canada, [9]Brookhaven National Laboratory, Upton, New York, USA, [10]Institute of Earth, Ocean, and Atmospheric Sciences Rutgers University, New Brunswick, New Jersey, USA, [11]Department of Chemistry and Biochemistry, University of Colorado Boulder, Boulder, Colorado, USA, [12]NASA ARC-CREST BAER, Moffett Field, California, USA, [13]National Park Service, Cape Cod National Seashore, Wellfleet, Massachusetts, USA

Abstract The Two-Column Aerosol Project (TCAP), conducted from June 2012 through June 2013, was a unique study designed to provide a comprehensive data set that can be used to investigate a number of important climate science questions, including those related to aerosol mixing state and aerosol radiative forcing. The study was designed to sample the atmosphere between and within two atmospheric columns; one fixed near the coast of North America (over Cape Cod, MA) and a second moveable column over the Atlantic Ocean several hundred kilometers from the coast. The U.S. Department of Energy's (DOE) Atmospheric Radiation Measurement (ARM) Mobile Facility (AMF) was deployed at the base of the Cape Cod column, and the ARM Aerial Facility was utilized for the summer and winter intensive observation periods. One important finding from TCAP is that four of six nearly cloud-free flight days had aerosol layers aloft in both the Cape Cod and maritime columns that were detected using the nadir pointing second-generation NASA high-spectral resolution lidar (HSRL-2). These layers contributed up to 60% of the total observed aerosol optical depth (AOD). Many of these layers were also intercepted by the aircraft configured for in situ sampling, and the aerosol in the layers was found to have increased amounts of biomass burning material and nitrate compared to aerosol found near the surface. In addition, while there was a great deal of spatial and day-to-day variability in the aerosol chemical composition and optical properties, no systematic differences between the two columns were observed.

1. Introduction and Motivation

The largest magnitude of the uncertainty associated with anthropogenic aerosol radiative forcing in regional and global models is found downwind of the primary urban emission sources, including the eastern edges of Asia, Europe, and North America [e.g., *Myhre et al.*, 2013; *Schulz et al.*, 2006]. Recent efforts have also pointed out the importance of elevated (in terms of altitude) aerosol layers on the Earth's radiation budget due to their impact on the vertical distribution of the scattering and absorption of sunlight by aerosol. For example, *Samset et al.* [2013] show that much of the differences in radiative forcing among 12 different global models can be attributed to differences in the vertical profiles of black carbon (BC) aerosol. To better constrain regional and global models and to better understand the importance of aerosol mixing state (i.e., mixtures ranging from external mixtures, in which each particle consists of a single compound, to internal mixtures, in which each particle consists of a range of different compounds) and its effect on aerosol optical properties, field studies are needed to characterize aerosol chemical and optical properties over a deep layer of the atmosphere in the geographic regions where anthropogenic effects are expected to be largest and model uncertainties are a significant concern.

The U.S. Department of Energy's Two-Column Aerosol Project (TCAP) was designed to use both surface and airborne systems to provide key measurements of aerosol composition (including particle mixing state), aerosol size distributions, and optical properties (both local and columnar), and the cloud macrophysical and microphysical properties that are needed to evaluate both detailed process models and three-dimensional atmospheric models. The field campaign was designed to examine conditions within two atmospheric columns. The first column was located over Cape Cod, Massachusetts, while the location of the second column varied with conditions and was located several hundred kilometers away from Cape Cod over the Atlantic Ocean. The distance between the columns was selected so that they would be in different model grid columns for the current generation of global models so that their performance in simulating horizontal gradients in aerosol microphysical and optical properties could be quantified.

The region downwind of New England has been the subject of several different studies prior to TCAP. The 2004 New England Air Quality Study (NEAQS) was part of the larger International Consortium for Atmospheric Research on Transport and Transformation (ICARTT) campaign, which included nine aircraft from North America and Europe, and was focused on measuring the impact of North American anthropogenic emissions and eastward transport of pollutant plumes from North America [*Fehsenfeld et al*., 2006]. One relevant finding of NEAQS was that a large amount of the pollutant transport occurs above an altitude of 3 km, so that surface measurements alone cannot be used to define the net exchange of gases and aerosol. In their analysis of ICARTT data, *Neuman et al*. [2006] reported finding well-defined plumes between the top of the marine boundary layer and an altitude of 3 km, with most plumes found at an altitude of 1.5 km or lower.

The 1996 Tropospheric Aerosol Radiative Forcing Observational Experiment (TARFOX) was conducted over the western Atlantic Ocean with a focus on reducing uncertainties of the effects of aerosols on climate. TARFOX included measurements of the chemical, physical, and optical properties of aerosol [*Hobbs*, 1999; *Russell et al*., 1999a; *Russell et al*., 1999b]. One of the primary findings of TARFOX was the relative importance of carbonaceous aerosol and aerosol water on the column aerosol optical depth (AOD) [*Hegg et al*., 1997; *Russell et al*., 1999a]. Data collected during TARFOX were also used to document the relative importance of aerosol layers, aerosol optical properties [*Redemann et al*., 2000b], and their impact on radiative forcing [*Redemann et al*., 2000a]. Based on their studies of observed and modeled aerosol forcing, *Hignett et al*. [1999] concluded that additional work was needed to fully examine the impact of aerosol mixing state on radiative forcing. One drawback of this early TARFOX study was the lack of instrumentation available at that time to adequately characterize the aerosol mixing state. Changes in power-plant emissions of sulfur dioxide, which occurred after 2000, have also likely altered the aerosol mixing state and radiative forcing in the region that climate models must accurately represent.

TCAP was designed to build on the experience of these important previous studies in a number of ways. First, the TCAP flight patterns were designed to be very simple and repeatable with very close coordination between the two aircraft that were used in the study. Rather than following a specific plume, aircraft missions focused on profiles of aerosols and their precursors within two columns. Second, a number of new instruments were deployed during TCAP that were not available during the previous studies, including an advanced NASA airborne sun photometer (the Spectrometer for Sky-scanning Sun-Tracking Atmospheric Research (4STAR)) [*Dunagan et al*., 2013; *Segal-Rosenheimer et al*., 2014; *Shinozuka et al*., 2013] and the second generation NASA High Spectral Resolution Lidar (HSRL-2) [*Müller et al*., 2014]. Other instruments developed since TARFOX and NEAQS that were deployed, such as single-particle mass spectrometers, allow measurements of the chemical properties and mixing state of individual particles, enabling an unprecedented look at aerosol chemical and optical properties off the east coast of the United States. TCAP included the deployment of the Atmospheric Radiation Measurement (ARM) Mobile Facility (collectively AMF), a well-instrumented surface site, which operated nearly continuously from June 2012 through June 2013 to provide information about the annual cycle of aerosol and clouds in the Cape Cod column. Finally, TCAP was designed to include both summertime (July) and wintertime (February) intensive observation periods (referred to as Phase 1 and Phase 2 hereafter). Previous field campaigns that focused on aerosol properties have often been conducted only during a portion of the summer. One expects a large annual cycle of aerosol chemical composition and mass loading [e.g., *Adhikary et al*., 2007; *Zhang et al*., 2007] and consequently aerosol optical properties due to seasonal changes in emissions, ambient meteorological conditions, and the amount of sunlight available for photochemistry.

This manuscript has four primary goals: (1) to provide an overview of the motivation for TCAP and document the instrumentation deployed as part of the study, including a description of the relevant sampling strategies

focused on summertime conditions (Phase 1, section 2); (2) to place TCAP into the larger context of previous field studies in the same geographic area, quantify differences in the aerosol loading, chemical composition, and optical properties in the two columns and at different altitudes, and illustrate the importance of air-mass history in interpreting the TCAP results (section 3); (3) to investigate the frequency of occurrence and the impact of aerosol layers aloft on the aerosol optical depth (AOD) over the study area during Phase 1 (section 4); and (4) to point to future research efforts involving the TCAP data sets needed to better characterize the sources of uncertainties in simulated aerosol radiative forcing, improve the treatment of aerosol lifecycle in climate models, and better understanding of cloud-aerosol interactions (section 5).

2. Phase I Description

The instrumentation deployed during TCAP was provided by the Department of Energy's Atmospheric Radiation Measurement (ARM) program and included the deployment of the AMF [*Mather and Voyles*, 2012] and ARM Aerial Facility (AAF) [*Schmid et al*., 2014], which included the Department of Energy (DOE) Gulfstream 1 (G-1) during Phases 1 and 2 and the NASA Langley King Air during Phase 1 only and additional surface instrumentation deployed by teams of scientists from NOAA, the University of Colorado, and the Massachusetts Institute of Technology. Complete descriptions of instruments deployed with the AMF over the course of the entire study period and on the research aircraft during Phase 1 are presented in Tables S1–S3 in the supporting information.

Throughout TCAP, the near-shore column was fixed over the Highland Center in the Cape Cod National Seashore and is referred to as the "Cape Cod column." During Phase 1, the second column was located over the Atlantic Ocean approximately 200 km away from the first column (Figure 1) and is referred to as the "Maritime column." The second column was not fixed in space but rather was arranged to be either approximately downwind of the first column or across an anticipated aerosol gradient. Each column was sampled at a number of different altitudes ranging from 100 to 200 m above the surface to approximately 4 km above sea level using in situ instruments aboard the G-1 aircraft, up to 8 km using the HSRL-2 on the King Air aircraft, and to the top of the atmosphere using the 4STAR. The exact G-1 sampling altitudes varied from flight-to-flight such that in situ measurements were made near the surface as well as in aerosol layers aloft. Between the two columns, the G-1 aircraft sampled in situ the lowest levels of the atmosphere (from 100 to approximately 500 m above the surface). The specific flight days and their orientation are given in Table 1, and the individual G-1 flight paths are shown in Figure 1.

2.1. Phase 1 Aircraft Instrumentation

Two research aircraft were deployed by the AAF during Phase 1: the DOE Gulfstream 1 (G-1) and the NASA Langley Research Center King Air. The G-1 was configured to make in situ measurements of aerosol optical properties, aerosol chemical composition, aerosol and cloud (both liquid and solid) particle-size distributions, cloud condensation nuclei (CCN) number concentrations, and trace gases as well as meteorological variables such as wind speed, wind direction, temperature, and humidity. The G-1 was also equipped with the 4STAR that can be used to measure the wavelength dependence of AOD for the depth of the atmosphere above the G-1 as well as a number of other variables. A detailed list of instrumentation deployed on the G-1 is presented in Table S3, and key instruments are described in more detail in section 2.2.1. The King Air was equipped with two downward looking remote sensors, the HSRL-2, and the Research Scanning Polarimeter [*Cairns*, 2003; *Knobelspiesse et al*., 2011] and flew a flight pattern along the same track as the G-1 but at a higher altitude of approximately 9 km. The HSRL-2 is described in more detail in section 2.1.2.

The flight patterns used during TCAP Phase 1 were developed to provide measurements at a number of altitudes in two atmospheric columns and were highlighted by the high degree of collaboration between the two aircraft. On each flight the King-Air repeated a simple back-and-forth pattern above the G-1, similar to the strategy used during the Cumulus Humilis Aerosol Processing Study [*Berg et al*., 2009]. In contrast to some studies conducted in the region [e.g., *Zaveri et al*., 2010], TCAP was not designed as a Lagrangian study, and no effort was made to explicitly find the pollutant plumes downwind of Boston or any other city. All of the research flights were anchored at one end to the AMF site. The second column was selected on the day before each flight based on the forecast of near-surface wind direction with the goal of sampling either along the mean wind direction (along the general direction of transport), or across wind (across expected aerosol gradients). It is important to note that in instances with large changes in the wind direction with height, the source region

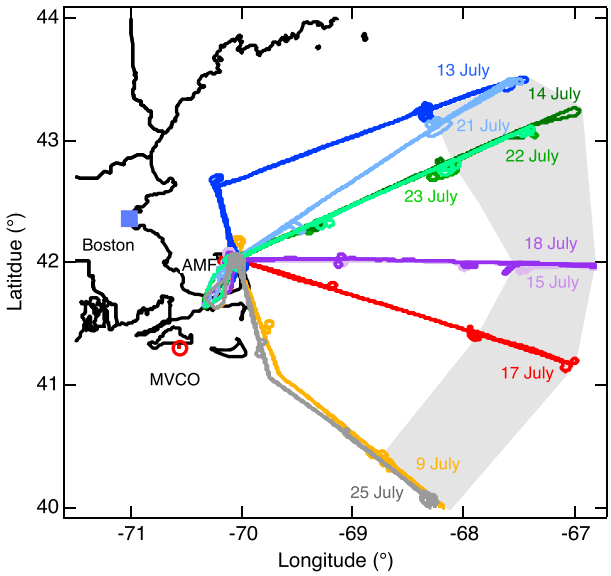

Figure 1. In situ G-1 flight tracks flown during TCAP Phase 1, with locations of the maritime columns indicated by the shading and line colors indicating different days. The King Air flight track was approximately the same as the G-1 track on any given day. The location of the Martha's Vineyard AERONET site (red circle) is shown for reference. The AMF was located at the Highlands Center, Cape Cod National Seashore, MA.

for aerosol in the residual layer and layers aloft could be quite different. The altitudes flown by the G-1 within both columns were determined in real-time using the in situ data and with guidance from the operators of the HSRL-2 on the King Air. This flexibility allowed the G-1 to sample within aerosol layers aloft detected by the HSRL-2. During the portion of the flight between the two columns, the G-1 flew within or just above the maritime boundary layer sampling the aerosol properties within 500 m of the ocean surface.

2.1.1. Gulfstream 1 (G-1)

The instrument payload on the G-1 was selected to provide detailed information about the aerosol chemical composition, particle-size distribution, and aerosol optical properties. Aerosol chemical composition was measured using an Aerodyne High-Resolution Time-of-Flight Aerosol Mass Spectrometer (HR-ToF-AMS, i.e., AMS), a single particle mass spectrometer, miniSPLAT [*Zelenyuk et al.*, 2015], and a particle-into-liquid (PILS) system. The amount of refractory BC (rBC) in the particle-size range of 100 to approximately 650 nm [e.g., *Lack et al.*, 2014] was measured using a Droplet Measurement Technology Single Particle Soot Photometer [SP2; *Moteki and Kondo*, 2007; *Schwarz et al.*, 2006]. It is important to note that the SP2 measures the rBC using an incandescence technique, while miniSPLAT determines the number fraction of soot-containing particles based on the individual particle's mass spectra [*Zelenyuk et al.*, 2015]. In the context of this work, we will consider these two measurements to be of similar material.

An Aerodyne AMS measures the chemically resolved submicron nonrefractory particle mass loading (noting that the AMS is unable to measure rBC) [*DeCarlo et al.*, 2006; *Jayne et al.*, 2000]. The AMS was operated only in the V-Mass Spectrometer (V-MS) mode to maximize sensitivity and temporal resolution, but eliminating the possibility of measuring size-resolved composition. Sample air was drawn from a one fourth inch stainless steel pickoff line inserted into the center of the G-1 aerosol isokinetic inlet flow. To maintain a constant sample flow through the instrument at each altitude, a pressure control inlet (PCI) was added upstream of the AMS aerodynamic lens. The PCI reduced the pressure upstream of the lens to approximately 620 mb by pumping a variable flow across a 200 μm orifice. A second 130 μm orifice operating under critical flow conditions is used to meter 1.4 cc s^{-1} of sample flow into the AMS. The orifice sizes were chosen such that sample flow through

Table 1. Flight Dates, Wind Direction, and Cloud Cover During the TCAP Phase 1 Intensive Observation Period (July 2012)

Date and Time (UTC) in 2012	Wind Direction and Cloud Cover
9 July, 16:59–20:26	Northwesterly winds and cirrus over flight track.
13 July, 14:58–19:05	Southwesterly winds and cirrus over flight track.
14 July, 17:10–20:19	Southwesterly winds and cirrus over flight track.
15 July, 14:01–17:20	Southwesterly winds. Cirrus over AMF, clear over second column.
17 July, 13:58–17:24	Southwesterly winds. Clear conditions.
18 July, 13:58–17:20	Northwesterly winds. Broken clouds over the flight track.
21 July, 17:04–20:08	Easterly winds. Cirrus over AMF, clear over second column.
22 July, 14:27–17:38	Southwesterly winds. Clear conditions
23 July, 14:00–17:15	Southwesterly winds. Cirrus over flight track.
25 July, 13:59–17:31	Northwesterly winds. Clear conditions.

the AMS was identical to the flow at sea level and room temperature. Signal intensity is converted to aerosol loading using standard procedures documented in the literature, either using unit mass resolution (UMR) signal processing [*Allan et al*., 2004; *Jimenez et al*., 2003] or high-resolution signal processing [*Aiken et al*., 2007]. The instrument ionization efficiency was regularly calibrated during the campaign using standard procedures and monodisperse ammonium nitrate particles. Calibrations were stable during the campaign, so all calibrations were averaged and a single calibration value was applied to all flight data. To account for real-time changes in the instrument, the signal intensity at m/z 28 (N_2^+) was normalized to the average value of the same signal obtained during calibration runs to generate a real-time correction factor (i.e., the "airbeam correction") that was applied to in-flight data. Sample flow was periodically diverted through a HEPA filter during each flight to remove particles from the airstream. Data collected during these filter periods were used to adjust the standard AMS fragment table for interference from gas-phase species [*Allan et al*., 2004].

In addition to the AMS, a single particle mass spectrometer, miniSPLAT [*Zelenyuk et al*., 2015], was deployed on the G-1. Unlike the AMS that provides information on the bulk aerosol composition, miniSPLAT measures the vacuum aerodynamic diameter (d_{va}) and composition of individual particles from 50 to 2000 nm in aerodynamic diameter. The miniSPLAT works on the same scientific principles as SPLAT II [*Zelenyuk et al*., 2009], but has been significantly reduced in both size and weight to improve its suitability for aircraft use [*Zelenyuk et al*., 2015].

The miniSPLAT is described in detail elsewhere [*Zelenyuk et al*., 2015]; here we give a brief overview of the relevant points. It uses an aerodynamic lens inlet to form a low divergence particle beam and transports the particles into the vacuum system with extremely high efficiencies. The aerodynamic lens imparts each particle with a velocity that is a narrow function of the particle's d_{va}. Two optical detection stages are used to determine particle velocity, and thus its d_{va}, and to generate a timed size-dependent trigger that fires the desorption/ionization excimer laser. The resulting mass spectra of volatile and nonvolatile fractions of individual particles are acquired using a dual-polarity Z-configuration time-of-flight (Z-TOF) mass spectrometer.

In addition to these measurements of single particle sizes and compositions, miniSPLAT provides information on the number concentrations of particles larger than 100 nm in diameter, particle, size distributions, densities, and asphericity at a rate determined by the ambient particle number concentrations and instrument detection efficiency [*Vaden et al*., 2011a, 2011b].

The measurements of particle density are especially useful when applied to composition-resolved size distributions. These densities, together with the mass spectra, are used to obtain quantitative information on individual particle compositions and to determine relative amounts of components in internally mixed particles [*Earle et al*., 2011; *Vaden et al*., 2011b; *Zelenyuk et al*., 2010].

TCAP Phase 1 was the first field deployment of miniSPLAT. It was used on all 10 research flights, sized approximately 32 million individual particles, and characterized size and mixing state of about 250,000 particles. While the vast majority of aerosol particles were composed of oxygenated organics mixed with various amounts of sulfates, as will be discussed later, miniSPLAT also detected and characterized fresh and aged soot particles, biomass burning aerosol, organic amines, as well as a small number of dust and sea-salt particles [*Zelenyuk et al*., 2015].

2.1.2. King Air

NASA Langley recently developed the first airborne multiwavelength high spectral resolution lidar (HSRL). This instrument, called HSRL-2 (the second-generation HSRL), is an advanced version of the airborne HSRL-1 instrument [*Hair et al*., 2008] that has acquired aerosol and cloud profiles on over 350 flights conducted on numerous field missions since 2006. In addition to implementing the HSRL technique at 532 nm as done on HSRL-1, the HSRL-2 also implements the HSRL technique at 355 nm, thereby enabling independent, unambiguous retrievals of aerosol extinction and backscatter at both wavelengths. It also employs the standard backscatter technique at 1064 nm and is polarization-sensitive at all three wavelengths. Consequently, HSRL-2 provides profile measurements of aerosol extinction and optical thickness via the HSRL technique at 355 and 532 nm, and profile measurements of aerosol backscatter and depolarization at 355, 532, and 1064 nm. Data are acquired at 15 m vertical and 0.5 s temporal resolution. The vertical resolution of the derived aerosol backscatter coefficients and depolarization measurements are 15 m, and the temporal averaging is 10 s (about 1 km horizontal) [*Rogers et al*., 2009]. The aerosol extinction profiles are computed at a vertical resolution of 150 m, and the temporal averaging is 60 s (about 6 km horizontal) [*Rogers et al*., 2009].

The vertical and horizontal resolutions can be varied to suit different applications. These data sets are utilized to better understand the aerosol properties through the entire column and will provide valuable information for evaluating the performance of both regional and global scale models in regards to aerosol optical properties as well as the vertical distribution of aerosol.

2.2. ARM Mobile Facility (AMF) Instrumentation

The AMF [*Mather and Voyles*, 2012] was deployed at the base of the Cape Cod column to document the meteorological and aerosol properties within the column during the full 1 year deployment and to provide the context for the airborne observations by the AAF aircraft. The AMF includes over 46 instruments or instrument systems (Table S1) and has been utilized at a number of locations around the globe since its first deployment in 2005 [e.g., *Berkowitz et al*., 2011; *Li et al*., 2011; *Miller and Slingo*, 2007; *Slingo et al*., 2008]. The AMF includes a unique suite of cloud radars, which include a dual-frequency, scanning W band (95 GHz) and Ka band (35.3 GHz) radar, and one profiling W band radar. The suite of cloud radars provides an unprecedented set of measurements of the cloud properties near the eastern seaboard of North America. The scanning ARM cloud radars (SACR) [*Kollias et al*., 2014a] were added to the AMF in September 2012, and TCAP marks their first operational deployment with the AMF, and details related to the radars are presented in section 5. The AMF includes a full suite of radiometric measurements to fully characterize the surface radiation budget, including a Cimel Sunphotometer and Multi-Filter Rotating Shadow Band Radiometer (MFRSR), which can be used to determine the AOD during clear-sky conditions. During TCAP, a second modified MFRSR and a downward facing multifilter radiometer were deployed by NOAA from 9 July through 6 September 2012. This system included an additional long-wave channel at 1623 nm. The Cimel Sunphotometer operated by ARM is identical to those deployed as part of the Aerosol Robotic Network (AERONET).

The AMF includes a suite of instruments, called the Aerosol Observing System (AOS), for measuring particle size and concentration, hygroscopicity, number of cloud condensation nuclei (CCN), and aerosol optical properties. The AOS samples continuously employ two impactors to remove particles larger than either 1 μm or 10 μm in diameter, respectively, from the sampling stream. The configuration of the ARM AOS is described in detail by *Sheridan et al*. [2001], and a list of instruments can be found in Table S1. The AOS was designed to provide long-term measurements of key aerosol parameters with minimal involvement from operators.

Recently, the ARM program developed the freestanding Mobile Aerosol Observing System (MAOS). The MAOS was designed to provide detailed measurements of aerosol properties and trace gas chemistry over time periods on the order of several months. During TCAP, the MAOS was operated during Phase 1 and Phase 2 to coincide with the deployment of the research aircraft. The suite of instruments, listed in Table S2, provides measurements of particle-size distributions from 15 nm to 1 μm using a Scanning Mobility Particle Sizer (SMPS) and ultra-high sensitivity aerosol spectrometer (UHSAS), CCN number concentrations, and aerosol optical properties (including three independent measurements of aerosol absorption coefficient and hygroscopicity measurements of aerosol growth and light scattering). Measurements were also made of the particle chemical composition, including refractory black carbon (rBC), and an extensive suite of research-grade instruments were used to measure trace gas aerosol precursors, carbon monoxide, oxides of nitrogen, sulfur dioxide, and ozone (Table S2). TCAP marks the second deployment of the MAOS and its first deployment with the AMF. During TCAP, the MAOS observations were enhanced with an Aerodynamic Particle Sizer (APS) to measure the aerosol size distribution for particles as large as 20 μm. It should be noted that the transmission efficiency of the MAOS system is 50% for particles approximately 8–9 μm in diameter, and there was no special consideration for line losses of large particles in the APS measurements.

Additional measurements of meteorological variables include a surface weather station, a Doppler sodar, Doppler lidar, and a radar wind profiler (RWP) that can be used to provide profiles of wind speed and wind direction from the surface to the boundary-layer top, augmenting other measurements made by the AMF. The profile of wind speed, wind direction, and atmospheric thermodynamics were provided by radiosondes, which were launched 4 times a day throughout the AMF deployment.

The ARM program encourages the deployment of additional instruments at its fixed or mobile sites that augment the standard instrumentation. During Phase 1 of TCAP a team of scientists from the University of Colorado deployed two innovative differential optical absorption spectroscopy (DOAS) instruments: (1) the two-dimensional (2-D) multi axis DOAS (2D-MAX-DOAS) instrument [*Coburn et al*., 2011; *Ortega et al*., 2015]

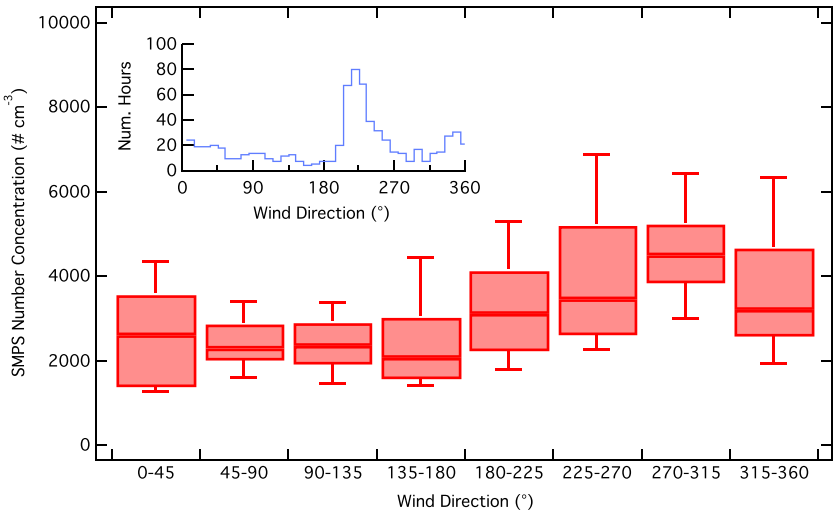

Figure 2. Box-and-whisker plots of particle loading for particles between 15 and 450 nm measured using the SMPS at the AMF site as a function of wind direction during July 2012. Whiskers indicate the 90th and 10th percentiles, and boxes indicate the 75th and 25th percentiles. The histogram of wind direction (inset) was measured at 100 m above the site using the Doppler lidar. Wind direction follows the standard meteorological convention so that northerly winds are from 0°.

that measures a number of trace gases in the column, including nitrogen dioxide (NO_2), glyoxal (CHOCHO), oxygen dimers (O_4), formaldehyde (HCHO) as well as the Raman scattering probability and the AOD and extinction profiles; (2) the light emitting diode cavity enhanced DOAS (LED-CE-DOAS) instrument [*Thalman et al.*, 2015; *Thalman and Volkamer*, 2010] that provides very sensitive near surface in situ measurements of NO_2, CHOCHO, and O_4 with 1 min time resolution.

2.3. WRF-Chem Configuration

To examine the air-mass history associated with the G-1 and King Air measurements, the Weather Research and Forecasting (WRF) model [*Skamarock et al.*, 2008] was run using two nested domains, an outer domain that encompasses most of North America with a horizontal grid spacing of 36 km and an inner domain that encompasses the northeastern United States and southeastern Canada with a horizontal grid spacing of 12 km. The simulation period was from 00 UTC 1 July to 00 UTC 26 July 2012. Initial and boundary conditions were based on the National Center for Environmental Prediction's Global Forecast System (GFS) model. Similar to, *Berg et al.* [2015], the parameterizations used include the Morrison microphysics scheme [*Morrison et al.*, 2009], the Kain-Fritsch deep convection scheme [*Kain*, 2004; *Kain and Fritsch*, 1990] coupled to the Cumulus Potential shallow convection scheme [*Berg et al.*, 2013], the Community Atmosphere Model (CAM) radiation scheme, the Mellor-Yamada-Janjić boundary layer scheme [*Janjić*, 1990, 2002], and the Noah land-surface scheme [*Chen and Dudhia*, 2001]. Four-dimensional data assimilation was applied above ~4 km above ground level (agl) using analyses from the GFS model so that the simulated synoptic conditions did not diverge from the observed large-scale meteorological conditions. Seven day back trajectories originating along the G-1 flight path at 1 min intervals (horizontal separation of approximately 6 km assuming a 100 m s^{-1} flight speed) were computed using the FLEXPART model [*Brioude et al.*, 2013] based on the WRF meteorological fields at hourly intervals.

2.4. General Meteorological Conditions

During Phase 1, the weather pattern over North America was dominated by a strong ridge of high pressure over the central U.S., leading to severe drought in parts of the Midwestern U.S. and increased precipitation over the Appalachian Mountains located in the mid-Atlantic states [*Blunden and Arndt*, 2013]. The area in the vicinity of Cape Cod, however, received near-normal amounts of precipitation during the study.

Meteorological conditions for the flight days are summarized in Table 1. The predominant wind direction 100 m above the surface at the AMF site (measured using the AMF's Doppler lidar) was from the south-southwest, with very few occurrences of winds from other directions (Figure 2). Flow from the southwest to northwest tended to have greater aerosol concentration, as measured by the SMPS deployed with the

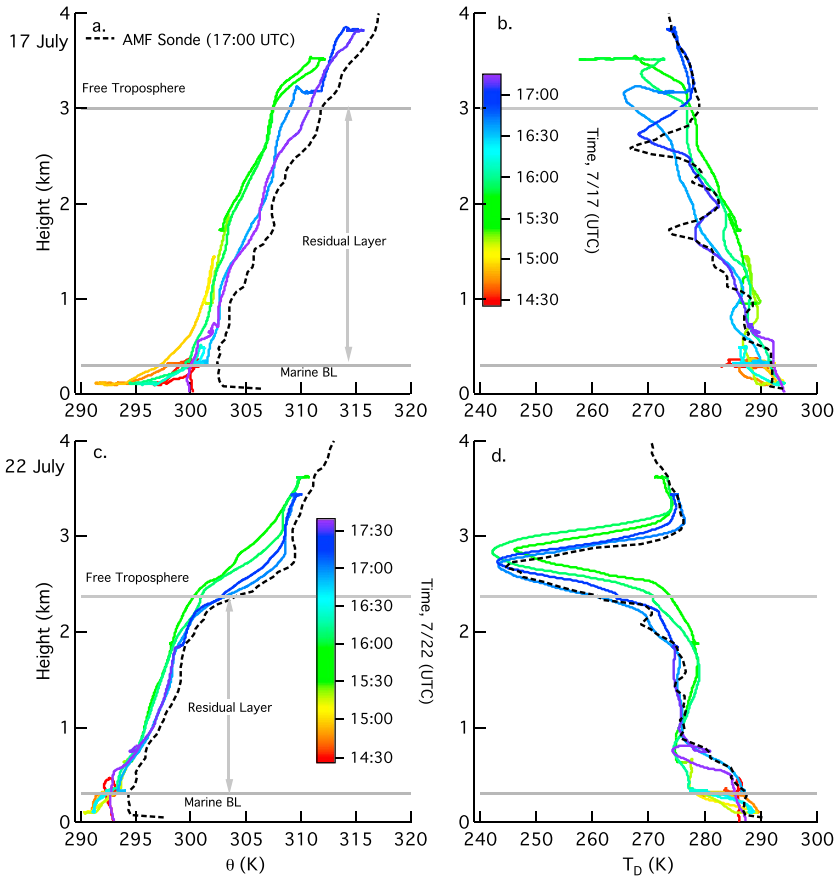

Figure 3. Profiles of (a, c) potential temperature (θ) and (b, d) dew-point temperature (T_D) measured on (Figures 3a and 3b) 17 July and (Figures 3c and 3d) 22 July using on board the G-1 (colors indicate time in UTC) and from the radiosonde launched at 17:00 UTC from the AMF site (dashed line). Orange and green colors correspond to the maritime column, while blue and purple indicate the Cape Cod column. The gray lines indicate the approximate boundaries of the marine boundary layer, residual layer, and free troposphere. Conditions are representative of Phase 1 flight days, and these and similar plots were used in conjunction with the HSRL-2 data to determine the residual layer depth.

AMF MAOS, than was seen in cases with other wind directions. It should be noted that while periods with easterly winds generally had smaller particle concentration, there are periods with flow from the east-northeast and east-southeast that were associated with particle number concentrations of approximately 3400 cm^{-3} (Figure 2). This can be explained by the presence of a sea-breeze circulation within an internal boundary layer that brings particle-laden continental air that has advected over the Atlantic Ocean back to the field site at the base of the Cape Cod column.

The thermodynamic structure of the lower atmosphere has been examined and was found to have similar characteristics on each of the 10 individual flight days during Phase 1. As an example, data collected on board the G-1 and radiosondes on 17 and 22 July are shown in Figure 3. The in situ observations of temperature and humidity show that the continental boundary layer was advected offshore with the prevailing westerly winds observed at the AMF site. During summer days, the ocean temperature is generally cooler than the temperature over land. Thus, the source of boundary-layer turbulence was turned off, as the air is advected over the ocean leading to the formation of a thick residual layer, similar to those that form over land during nighttime [e.g., *Stull*, 1988]. While the vertical profiles of potential temperature and particle loading appear well mixed within the residual layer, the layer was not turbulent (not shown). Often, a relatively shallow convective boundary layer several hundred meters thick was observed over the AMF site on Cape Cod, which was likely related to solar heating of the peninsula (as can be seen in the radiosonde temperature profiles in Figures 3a and 3c). Over the ocean a statically stable internal marine boundary layer formed was only several hundred

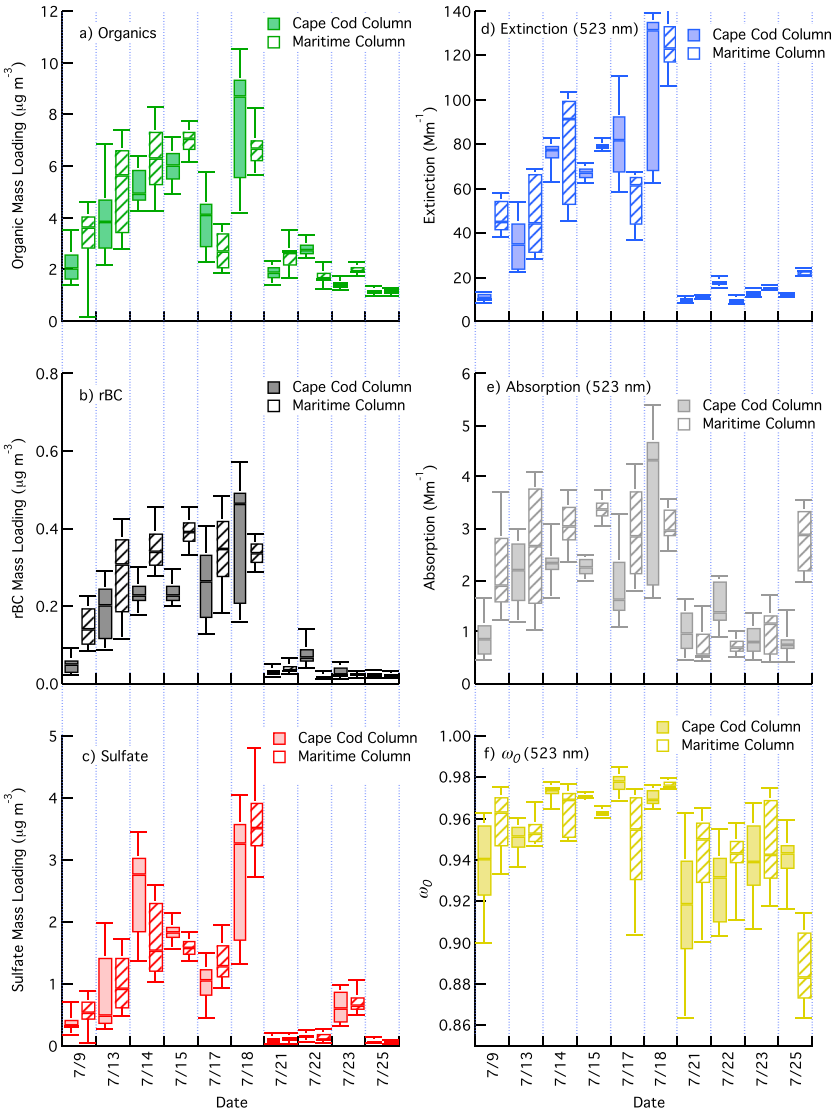

Figure 4. Mass loading of (a) organic, (b) rBC, and (c) sulfate as well as aerosol (d) extinction, (e) absorption, and (f) ω_0 for altitudes less than 400 m in the Cape Cod (solid) and Maritime (hashed) columns. Box-and-whisker plots indicate the 95th, 75th, 50th, 25th, and 5th percentiles.

meters deep (Figure 3). In the context of this study, the residual layer was identified visually using plots of aerosol backscatter measured by the HSRL-2 in combination with the vertical profiles of potential temperature and humidity measured by the G-1 and radiosondes.

3. Analysis of Selected Observations From Phase 1

One of the goals of TCAP was to observe aerosol properties under a wide variety of conditions, including periods with both large and small aerosol loading and to quantify systematic differences in the aerosol microphysical and optical properties observed within the Cape Cod and maritime columns.

3.1. Differences in Aerosol Properties in the Cape Cod and Maritime Columns

The analysis presented in this subsection includes data collected on straight and level flight legs flown at altitudes less than 400 m during each of the Phase 1 G-1 flights. This specific height range was selected to ensure that all of the observations included in this particular analysis were within the residual layer making day-to-day comparisons more meaningful. This treatment allows us to examine the variability of aerosol chemical

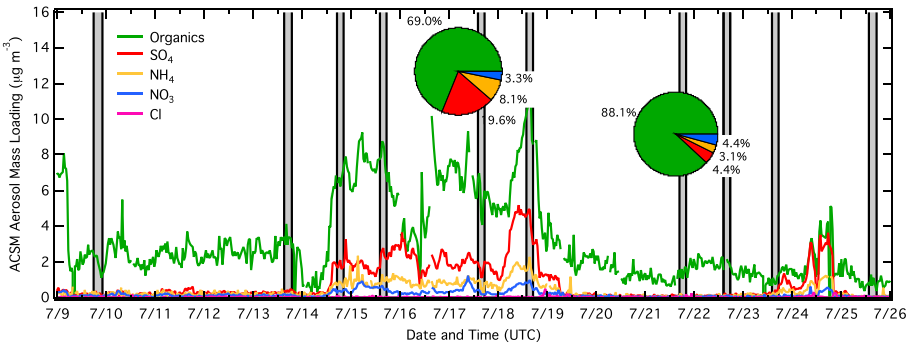

Figure 5. Aerosol mass loading of total organics, sulfate, nitrate, ammonium, and chloride measured by the ACSM at the AMF surface site. Shaded areas indicate periods with research flights by the G-1 and King Air. Pie charts indicate aerosol mass fractions measured at the AMF site during the time periods of the G-1 flights on 17 and 22 July.

and optical properties over the entire duration of Phase 1 as well as differences between the Cape Cod and maritime columns (Figure 4). A number of features are evident in Figure 4. First, the mass loading of organic, sulfate (measured by the AMS), and rBC (measured by the SP2) aerosol was much larger during the middle part of the study (14 through 18 July; Figures 4a–4c). Likewise, the aerosol extinction and absorption measured using the Particle Soot Absorption Photometer (PSAP) and nephelometer (with the measured light scattering adjusted using the measured Ångström exponent to match the wavelengths measured by the PSAP) are also larger on these days (Figures 4d and 4e). Compared to conditions observed from 14 through 18 July, the aerosol mass loading and optical properties are moderate during the flights conducted on 9 and 13 July. Between 18 and 21 July there is a significant decrease in the aerosol mass loading and associated decreases in the aerosol absorption and extinction. This behavior is consistent with the surface observations from the Aerosol Chemical Speciation Monitor (ACSM) deployed at the AMF site (Figure 5). Second, during the periods with small aerosol loading, the aerosol mass is dominated by organic aerosol with very small amounts of sulfate aerosol and rBC (Figures 4a–4c). Third, there is evidence of a decrease in ω_0 during the cleaner period in the second half of the study (Figure 4f), suggesting that the remaining aerosol mass is proportionally more absorptive than was seen in the first part of the study.

The data shown in Figure 4 also highlight the variability in the aerosol loading between the Cape Cod and maritime columns, which is a function of a number of different atmospheric processes, including aerosol aging and transport. However, there are no systematic differences between the mass loading and optical properties between the two columns. In other words, the Cape Cod column, which is closer to emission sources including Boston, can have either smaller or larger aerosol mass loading than was observed in the maritime column on any given day. For example, on 9 and 13–15 July the mass loading of organic aerosol, and rBC as well as the aerosol absorption and extinction are greater in the maritime column than in the Cape Cod column (Figure 4). In contrast, on 18 July the mass loadings of organic aerosol and rBC along with the aerosol absorption and extinction are smaller in the maritime column. There are also days for which there are differences in the spatial trends between the organics and sulfate between the two columns (Figures 4a and 4c). Similar spatial trends between the organic and sulfate loading (where both are either increasing or decreasing with distance from the Cape Cod column) were identified on 50% of the flight days. It is worth noting that there can be a great deal of variability within each individual column. An extreme example can be found for the organics on 18 July, where the 95th and 5th percentiles of organic aerosol span 6.3 $\mu g\,m^{-3}$ (Figure 4a). On that same day, however, the span is much smaller in the maritime column, where the difference between the 95th and 5th percentile is only 2.6 $\mu g\,m^{-3}$.

The differences in the dry (relative humidity less than 40%) extinction and absorption observed in the two columns are related to the aerosol mass loading as well as (to a lesser extent) the particle-size distribution (as will be discussed below). There is a large degree of similarity between the column differences in extinction and the organic mass loading (Figures 4a and 4d), which is not surprising given that organic aerosol dominates the total aerosol mass. As expected there is a high degree of correlation between the rBC and the absorption (Figures 4b and 4e), with the exception of conditions in the maritime column on 25 July. In this case the absorption measured using the PSAP in the column is much larger than that which is seen in the Cape Cod column, even

though there is little difference between the columns in regard to the mass loading of rBC (which is small in both cases). One possible explanation for this behavior is the presence of relatively large particles in the maritime column, which could be too large to be observed by the SP2 (which is only sensitive to particles as large as 0.6 μm in size [*Sedlacek et al.*, 2012]). The median value of the scattering Ångström exponent computed for the maritime column during this flight was 0.65. This is the smallest median value found during any of the TCAP Phase 1 flights (for comparison the median Ångström exponent in the Cape Cod column was 1.7 on 25 July) and is consistent with much smaller particles over land than in the maritime column.

The majority of aerosol seen during TCAP are weakly absorbing, and all but one of the median values of dry ω_0 were found to be larger than 0.92 (Figure 4f). In the first half of the study the aerosol extinction was generally more than an order of magnitude larger than the absorption (Figures 4d and 4e). In the second half of the study the extinction was still much larger than the absorption, but the average ratio of absorption to extinction is a factor of 1.8 and 2.0 larger in the Cape Cod and maritime column, respectively, during the latter flights. As a result, the median values of dry ω_0 are larger than 0.94 prior to 19 July, compared to median values as small as 0.88 after that same date (Figure 4f). The values ω_0 measured in situ are smaller than those derived using the MFRSR, which had a mean value of 0.986 [*Kassianov et al.*, 2013]. These differences are likely due to differences between the in situ measurements of dry aerosol and the aerosol optical properties at ambient conditions measured by the MFRSR.

3.2. Case Study of Aerosol Chemical Composition and Optical Properties

Two days, each with southwesterly near-surface winds at the AMF site (17 and 22 July 2012), have been selected for additional analysis to highlight the utility of the integrated TCAP data set and to show how these measurements can be combined to investigate a range of aerosol properties and their impact on the AOD. Both days were clear over Cape Cod (as confirmed by a review of images from the Total Sky Imager deployed the AMF site) and maritime columns (with the exception of some low-level stratus in the maritime column on 17 July), allowing us to compare the in situ observations and measurements from the remote sensing instruments.

The in situ data can be used to determine how the chemical composition of aerosol in both the residual layer and layers aloft varies, how it compares to observations made at the AMF site at the bottom of the Cape Cod column, and how it is related to the aerosol optical properties. The near-surface aerosol mass loading measured by the ACSM at the AMF was relatively large from 15 to 19 July 2012 and then decreased significantly (Figure 5). On 17 July the average mass loading of nonrefractory aerosol was 8.9 $\mu g\,m^{-3}$ compared to only 2.0 $\mu g\,m^{-3}$ on 22 July. This change in mass loading was accompanied by a change in the aerosol composition observed at the surface site. On 17 July, the aerosol measured by the ACSM at the surface site was a mixture of organics and sulfate with some ammonium and nitrate. By contrast, the mass fraction changed significantly on 19 July, and on 22 July it was dominated by organics with only very small amounts of sulfate and other components (Figure 5). There are some differences in the aerosol mass loadings measured at the AMF site and on board the G-1. The average aerosol mass loading observed on 17 July in the lowest leg over the Cape Cod column was 4.4 $\mu g\,m^{-3}$, which is about three quarters of that seen at the AMF site (5.9 $\mu g\,m^{-3}$), but the airborne measurement is a factor of 1.7 larger on 22 July (3.6 $\mu g\,m^{-3}$ measured on board the G-1 compared to 2.1 $\mu g\,m^{-3}$ measured at the AMF site). These differences are likely attributable to differences in the vertical structure of the aerosol and the air-mass history. The mass fraction of nonrefractory aerosol measured by the airborne AMS on 17 July is dominated by organics (73%), with 19% sulfate, 6% ammonium, and 3% nitrate at approximately 300 m above mean sea level (msl). The lowest altitude leg of the column on 22 July (also approximately 300 m above msl) is found to be higher in organics (82%), lower in sulfate (6%), and approximately the same in ammonium and nitrates (7% and 4%, respectively) when compared to conditions on 17 July. These values are in good agreement with the number fractions measured by miniSPLAT and ACSM at the AMF site (not shown).

The HSRL-2 data show the presence of aerosol layers aloft on both 17 and 22 July that are marked by increased amounts of aerosol backscatter (Figures 6, S1, and S2, please note the change in scale between the two figures). On 17 July there is a thick layer of large aerosol backscatter from the surface to an altitude of approximately 3 km along the entire flight track (Figures 6 and S1). This layer corresponds to the residual layer that is indicated by the potential temperature profile to extend from several hundred meters above the surface to an altitude of 4 km (Figure 3a). On 22 July there is an aerosol layer between an altitude of 3 and 5 km that spans the distance between the two columns with a residual layer below an altitude of approximately 2.5 km (Figures 6 and S2).

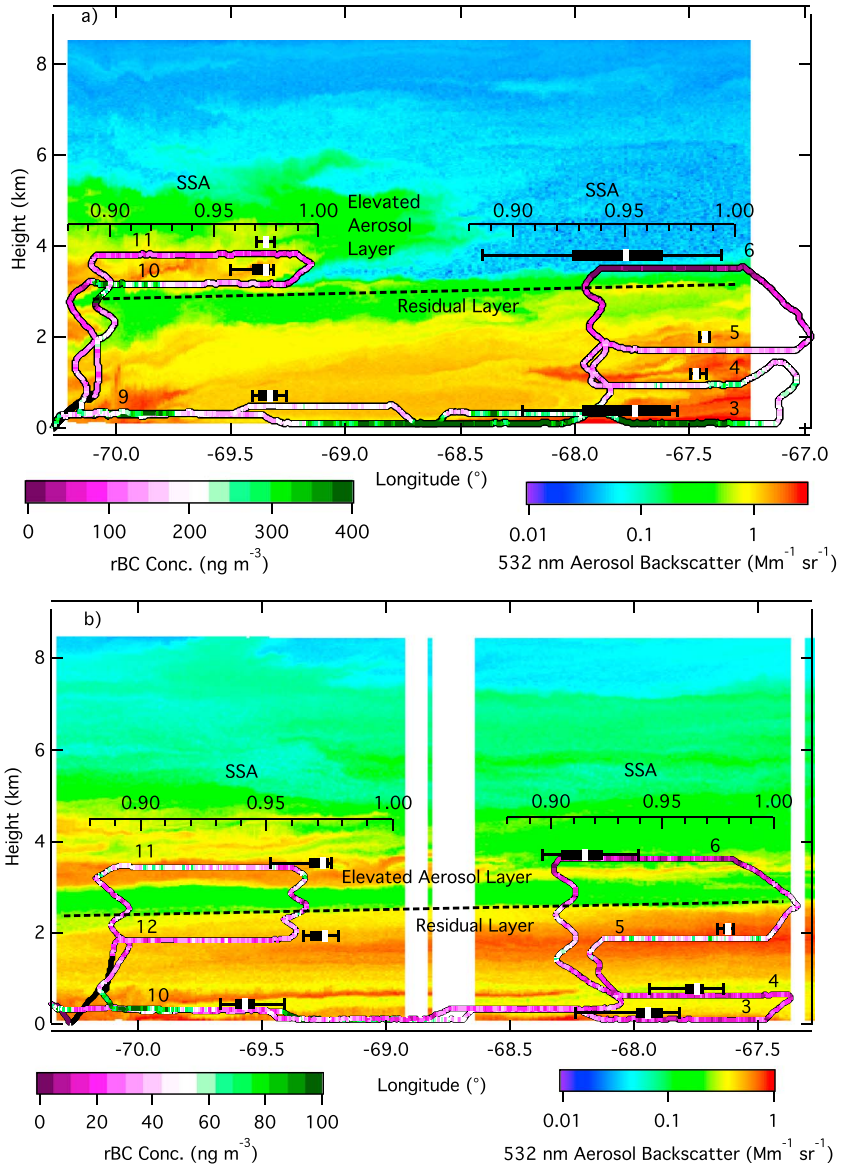

Figure 6. Aerosol backscatter at a wavelength of 532 nm measured by the HSRL-2 (background colors) for specific segments of the King Air flight and the entire G-1 flight path (color coded by rBC mass loading) on (a) 17 July (corresponding to Figure 7d) and (b) 22 July (corresponding to Figure 8b). Box-and-whisker plots (95th, 75th, 50th, 25th, and 5th percentiles) correspond to ω_0 distributions over the entire level transects indicated by the leg numbers. Dashed lines indicate the top of the residual layer.

The aerosol mass loading (including mass loading of rBC) and aerosol optical properties within the Cape Cod and maritime columns have a complicated vertical structure associated with the residual layer and aerosol layers aloft (Figure 6). The measurements of chemical composition are presented next in several different ways to document different aspects of the changes in the aerosol with both height and between the two columns. Box-and-whisker plots of mass loading showing the 90th, 75th, 50th, 25th, and 10th percentiles of aerosol composition concentration for the height bins that include the flight legs are shown in Figure 7 (AMS data) and Figure 8 (SP2 and miniSPLAT data) that quantify horizontal variability and vertical distribution within each column. The horizontal bar plots presented in Figure 9 show the relative number fractions of particles with different compositions and mixing states measured by miniSPLAT along the flight legs. These data show that the vast majority of individual aerosol particles were composed of internal mixtures of oxygenated organics and sulfate, labeled in Figure 9 by the fraction of sulfates (10, 15, or 30% weight fraction and the

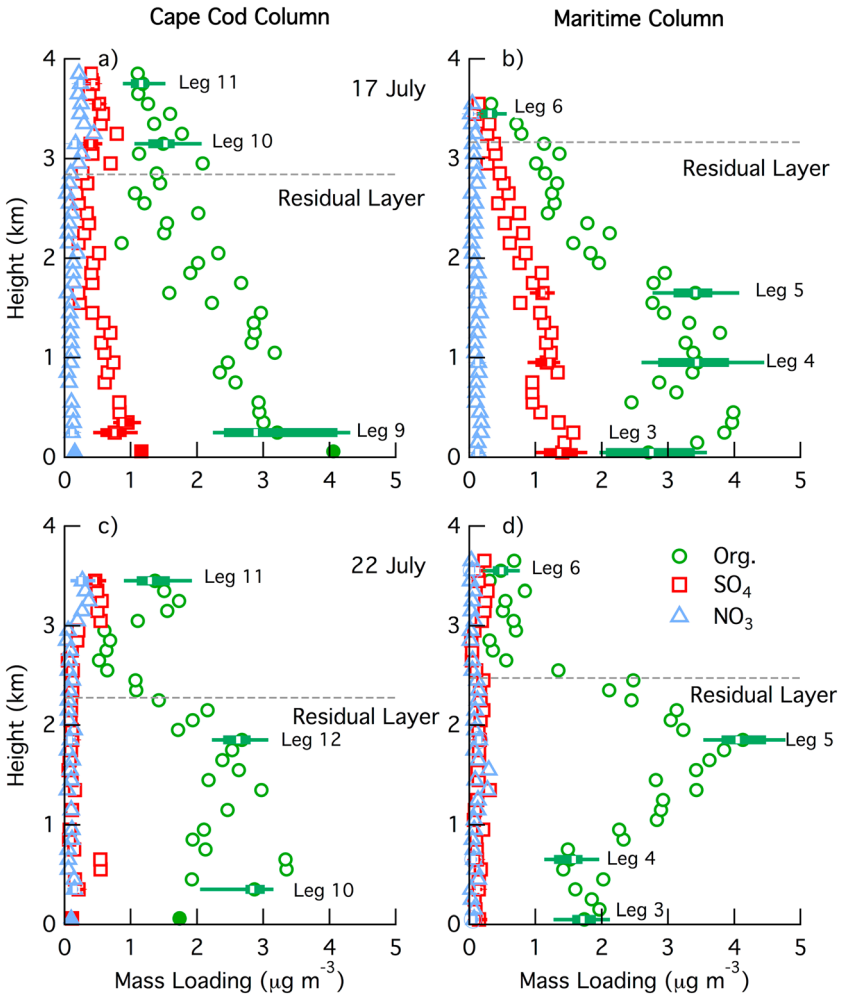

Figure 7. Mass loading of organics (green), sulfate (red), and nitrate (blue) measured by the airborne AMS on (a and b) 17 and (c and d) 22 July in the (Figures 7a and 7c) Cape Cod and (Figures 7b and 7d) maritime columns. Filled symbols near the base of the Cape Cod column represent surface measurements by the ACSM at the AMF site. Box-and-whisker plots indicate 90th, 75th, 50th, 25th, and 10th percentiles of mass loading along G-1 flight legs (labeled by leg number and corresponding to legs identified in Figure 9). Open symbols represent data taken during periods in which the aircraft was ascending or descending that have been binned into height bins 100 m thick.

dominant mass-spectral peak $m/z = 44$ or 43). In addition, miniSPLAT detected and characterized fresh and aged soot particles, biomass burning (BB) aerosol, organic amines, and a small number of dust and sea-salt particles.

3.2.1. 17 July: Large Aerosol Loading

On 17 July the mass loading of organics, sulfate, and rBC decreased steadily with height in the Cape Cod column through the top of the residual layer (Figures 7a, 7b, 8a, and 8b). The miniSPLAT data show that most observed particles consist of organics mixed with various amounts of sulfate, regardless of location or altitude (Figure 9, top). The aerosol layer aloft found above the residual layer that was sampled on Legs 10 and 11 on 17 July (Figure 9, top) has relatively large fractions of sulfate and nitrate when compared to measurements made in the residual layer, consistent with the AMS-measured mass loadings (Figures 7a and 7b). Based on increased levels of enhanced biomass burning particles, it is likely that the layer aloft is associated with long-range transport of aerosol produced, in part, by biomass burning as will be shown in section 5. In the maritime column on 17 July, the mass loading of organics remains large, as altitude is increased to 1.85 km, followed by a steady decrease through the top of the residual layer (Figures 7a and 7b). In contrast, the sulfate (Figures 7a and 7b) and rBC mass loadings (Figures 8a and 8b) and the relative fraction of soot particles and particles with higher sulfate content (Figure 9a) decrease steadily with increasing height from the ocean surface through the top

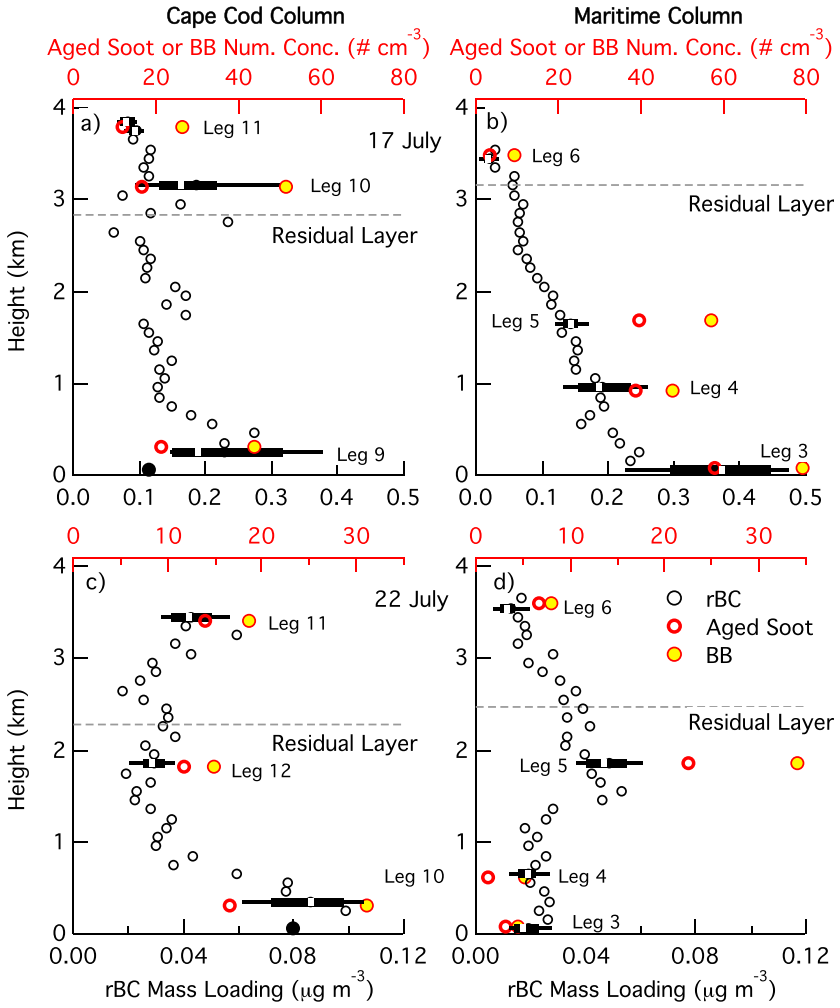

Figure 8. Mass loading of rBC (open circles) measured by the airborne SP2 and number fraction of aged soot (red circles) and biomass burning (BB) aerosol (yellow circles) measured by the airborne miniSPLAT on (a and b) 17 and (c and d) 22 July in the (Figures 8a and 8c) Cape Cod and (Figures 8b and 8d) maritime columns. Filled black symbols near the base of the Cape Cod column represent surface measurements by the SP2 at the AMF site. Box-and-whisker plots indicate 90th, 75th, 50th, 25th, and 10th percentiles of rBC mass loading along G-1 flight legs (labeled by leg number and corresponding to legs identified in Figure 6). Open symbols represent data taken during periods in which the aircraft was ascending or descending that have been binned into height bins 100 m thick.

of the residual layer. In contrast to the rBC, the median ω_0 values (calculated using data from the nephelometer and PSAP) for Legs 9, 10, and 11 on 17 July in the Cape Cod column are nearly the same despite the larger rBC concentration observed in Leg 9 (Figure 6a) indicative of changes in both the rBC and mass loading of less absorptive aerosol. Leg 3, close to the ocean surface, has a high mass loading of rBC, and small values of ω_0, (Figure 6a) well as larger number concentrations and larger relative number fractions of both aged soot and biomass burning aerosol (Figure 9a). It is likely that this leg intercepted a ship plume. As expected, there is also a good correlation between the rBC and the aerosol absorption measured during the entire flight on 17 July measured using the SP2 and PSAP, respectively. On this day, the mass absorption coefficient (MAC—defined as the slope of the line in Figure 10) is found to be 7.4 $m^2 g^{-1}$, which is consistent with the value of 7.5 ± 1.2 $m^2 g^{-1}$ that has appeared in the literature [e.g., *Bond and Bergstrom*, 2006; *Clarke et al.*, 2004].

3.2.2. 22 July: Small Aerosol Loading

Data from the AMS on the G-1 and AMF ACSM indicate that the near-surface aerosol mass loadings were smaller on 22 July than on 17 July (Figures 4 and 5). Data collected on the G-1 on 22 July suggest that this observation is consistent with conditions through the entire Cape Cod column (Figure 7c). The aerosol number fractions

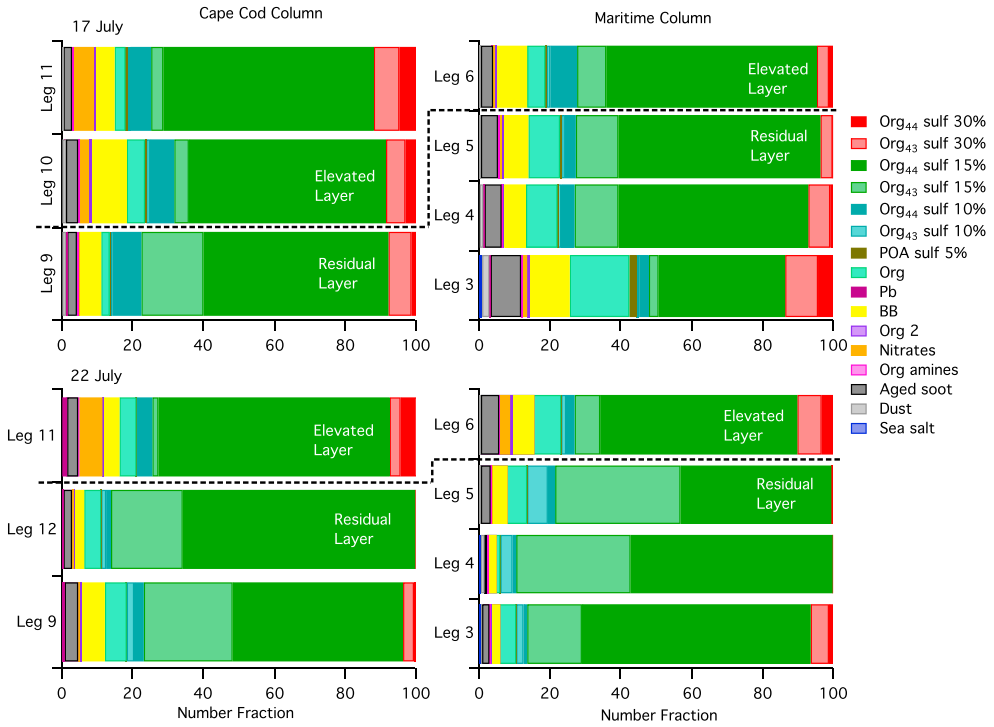

Figure 9. Number fraction of various aerosol chemical mixtures measured on board the G-1 in the Cape Cod and Maritime columns using miniSPLAT for specific legs identified in Figure 6 on (top) 17 July and (bottom) 22 July. Dashed black lines separate legs found in elevated layers and the residual layer.

(Figure 9, bottom) are again dominated by organics mixed with varying amounts of sulfate, although the number fraction of organics mixed with high levels of sulfate is much smaller than on 17 July, especially for Legs 4, 5, and 12. The mass loading of organics and sulfate is relatively constant with height in the Cape Cod column until the residual layer boundary is approached (Figures 7c and 7d), at which point it decreases. It is also important to note that the mass loading of rBC and number concentration of BB are much smaller on 22 July than is seen on 17 July. In the Cape Cod column on 22 July, the rBC mass loading and number concentration of biomass burning aerosol are, however, much larger near the bottom of the column (Leg 10) and decrease significantly, as

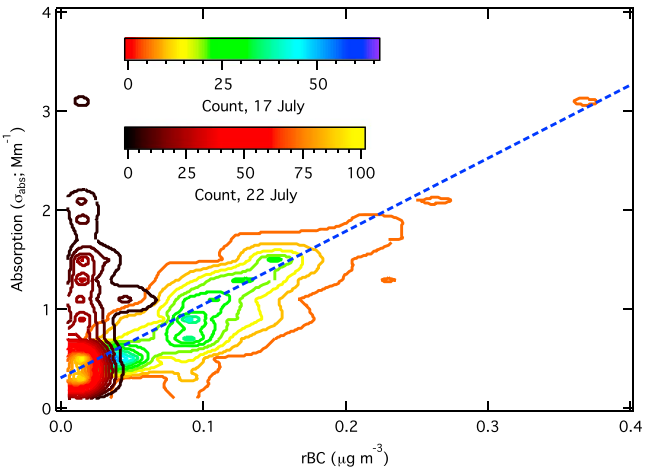

Figure 10. Distribution of aerosol absorption as a function of mass loading of rBC for (rainbow) 17 and (black yellow) 22 July measured at all attitudes along the G-1 flight track. The first contour interval represents a count of 5, and the contour interval is 5.

height is increased to 1 km. Within the maritime column, the organics mass loading is highest near the top of the residual layer (Figures 7c and 7d), and this section of the flight pattern (Leg 5) intersected a layer that is visible in the HSRL-2 data (Figure 6b). The layer has relatively large mass loading of rBC and large number concentrations of aged soot and biomass burning aerosol (Figures 8c and 8d) and is likely associated with forest fires and long-range transport of aerosol, which will be discussed in the next subsection. The number fraction of organics mixed with small amounts of sulfate is larger in this layer than was found at lower altitudes, but the number of particles with higher sulfate fractions is reduced. The aerosol layer aloft seen by the HSRL-2 above the residual layer appears to span both columns but is more pronounced in the Cape Cod column. Data collected by instrumentation on board the G-1 show that this layer has increased mass loading of sulfate, nitrate (as measured by the AMS), and rBC (as measured by the SP2), as well as larger number concentrations of biomass burning aerosol and to a lesser extent aged soot. This suggests that this layer is associated with long-range transport of aerosol to the Cape Cod column. However, little evidence is seen of increased mass loading of organic aerosol at this altitude in the maritime column. The increase in the relative fraction of absorbing aerosols (aged soot and BB particles) is consistent with the corresponding smaller ω_0 values found on Leg 6 (Figure 6b). The MAC ($7.4\,m^2\,g^{-1}$) derived from the PSAP measured absorption and SP2-measured rBC mass loading collected on 17 July is consistent with the majority of the aerosol observed on 22 July, as indicated by the large number of counts near the origin (Figure 10). Occasionally, there are observations for which the absorption coefficient ranges from 1 to $2\,Mm^{-1}$ for very small values of rBC (less than $0.05\,\mu g\,m^{-3}$). These points could be related to a number of different factors, including uncertainty in the PSAP measured absorption.

3.3. Model Back Trajectories

An analysis of 7 day back trajectories computed using WRF-Chem indicates differences in the air-mass history between the two columns on 17 and 22 July that can help explain the differences in aerosol loading and composition seen on the different days (Figure 11). On 17 July (Figure 11) the back trajectories from the Cape Cod column are initially from the northwest at all altitudes. In contrast, the initial low-altitude back trajectories in the maritime column are more convoluted. A slow moving high pressure system over the northeastern U.S. led to counter-clockwise circulation of air in the lower troposphere over the mid-Atlantic and New England states. The relatively long residence times over this region suggest that a buildup of aged aerosols from multiple anthropogenic, biogenic, and biomass burning emission sources over the northeastern U.S. contributed to the high aerosol extinction within the residual layer observed by the HRSL-2. The back trajectories also indicate that Boston is likely the largest anthropogenic source contributing to the residual layer aerosols over the AMF site, while other urban sources closer to New York City likely contribute a large fraction of aerosols within the maritime column. In contrast, the longer trajectories originating above the residual layer reflect the larger wind speeds in the free troposphere. These air masses pass over western Canada and the north central U.S. before arriving over the TCAP sampling region. The model suggests that the aerosol layer between 3 and 4 km msl over the AMF site was subject to biomass burning emissions from large fires in western Canada that occurred over several days prior to 17 July. This is consistent with a relatively large number fraction of biomass burning aerosol number concentration from miniSPLAT measurements within the aerosol layer aloft over the AMF site (Figure 8a). The air mass in the free troposphere over the maritime column also passes over the biomass burning sources in Canada, but at higher altitudes that are likely beyond the vertical extent of mixing and injection heights of the fires and therefore contains relatively small aerosol concentrations.

On 22 July (Figure 11e), the 7 day back trajectories indicate northwesterly winds above 1.5 km msl and easterly winds below 1.5 km msl. Within 1.5 km of the ocean, the back trajectories suggest a local recirculation was possible one to two days prior to the G-1 flight. Relatively low aerosol concentrations were observed close to the ocean surface since those back trajectories passed over eastern Quebec between 16 and 19 July where anthropogenic emissions are very small, and there were few fires. HSRL-2 measurements show thin layers of extinction within 1 km of the ocean, but the trajectory analysis indicates that these layers likely result from the recirculation of aerosol from local sources in Rhode Island and southern Massachusetts, either from small cities or small fires observed near the coast. The air mass above 1.5 km msl in the maritime column passes over Ontario and Quebec before being transported into the TCAP sampling region. The aerosol layer at approximately 2 km msl with the highest extinction over the maritime column also contained relatively large number fraction of biomass burning particles (Figure 8d). Many of the back trajectories originating at this altitude passed over large biomass burning sources in both eastern and western Ontario. Some of the

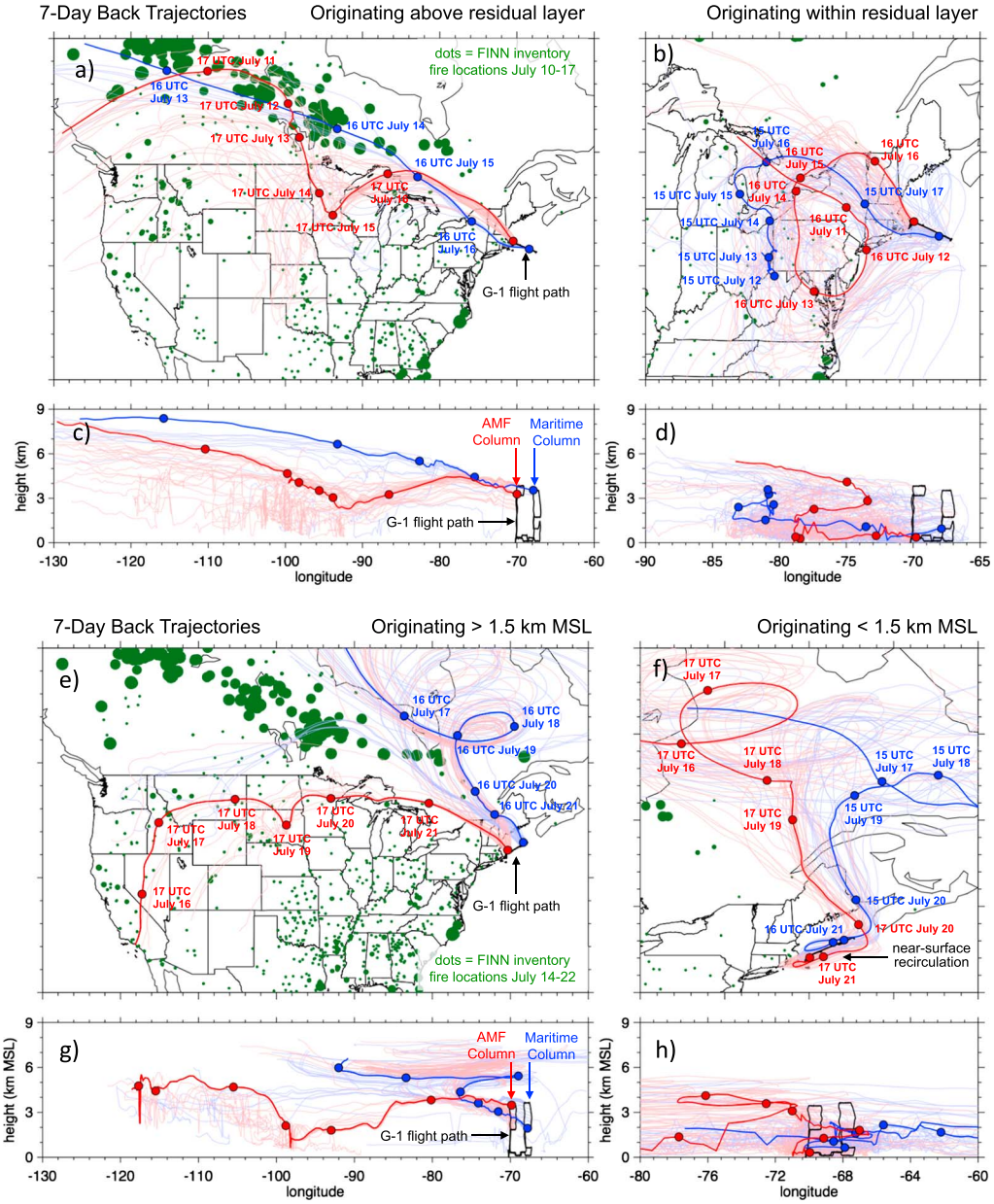

Figure 11. Back trajectories computed using the WRF model for the Cape Cod (red) and maritime (blue) columns on (a–d) 17 and (e–h) 22 July. Figures 11a and 11e indicate parcel trajectories for air parcels originating above the residual layer on (Figure 11a) 17 July or from heights greater than 1.5 km on (Figure 11e) 22 July with the location and magnitude of wildfires during the 7 days before the G-1 flight indicated by the location and size of the green dots. Dates indicate selected parcel locations along a typical trajectory. Figures 11b and 11f are similar, but for points originating within the residual layer on (Figure 11b) 17 July or from heights less than 1.5 km on (Figure 11f) 22 July. Figures 11c, 11d, 11g, and 11h are longitudinal cross sections consistent with the cross sections shown in the other panels.

trajectories for the Cape Cod column above 1.5 km are similar to those over the maritime column; however, a large fraction of trajectories also pass over the western U.S. where the fire sizes were much smaller than the Canadian fires. Therefore, the aerosol layer between 3 and 3.5 km msl over the AMF site had somewhat lower extinction and lower biomass burning number concentrations (Figure 8c) because of upwind mixing of different air masses, with many of the back trajectories having passed over the western U.S. where the fire sizes were much smaller than the Canadian fires.

3.4. Relationship to ICARTT and TARFOX

As described in section 1, the ICARTT study was focused on measuring trace gases and aerosol resulting from North American anthropogenic emissions and their eastward transport from North America to the northern Atlantic Ocean. Many of the ICARTT flight tracks encompassed the same region as the TCAP flights [*Fehsenfeld et al*., 2006], and it can be useful to compare a relevant subset of the ICARTT results with those from TCAP. The general thermodynamic structure of the atmosphere over the ocean was consistent during both studies, with a relatively thin stable layer observed near the ocean surface during TCAP (Figure 3) and ICARTT [e.g., *Angevine et al*., 2006]. The aerosol during ICARTT was also dominated by mixtures of organics and sulfate. *Murphy et al*. [2006] presented data collected using particle analysis by laser mass spectrometry at a number of locations around the globe, including observations from ICARTT, which showed that over 90% of the accumulation mode particles were a mixture of organics and sulfate. Similar results were found using miniSPLAT during Phase 1 of TCAP, where the vast majority of particles (median number fraction of 86% for observations made at altitudes less than 400 m) were composed of internal mixtures of organics and sulfate.

ICARTT also included the deployment of the R/V *Ron Brown* [*Fehsenfeld et al*., 2006], which was equipped with an AMS similar to the AMS on the G-1 and the ACSM deployed at the AMF site. Measured organic aerosol concentrations at the TCAP AMF site during Phase 1 ranged from values as small as 1 $\mu g\,m^{-3}$ to as large as 11 $\mu g\,m^{-3}$. The peak concentrations observed during TCAP are comparable to those observed on board the R/V *Ron Brown* during periods when sampling was conducted in urban plumes [*Quinn et al*., 2006]. The sulfate loading was generally smaller during TCAP than was seen during ICARTT (likely associated with changes in SO_2 emissions that occurred between 2004 and 2012 that are associated with changing air-quality regulations). The average sulfate mass loading measured at the AMF site was 0.78 $\mu g\,m^{-3}$ with a standard deviation of 0.86 $\mu g\,m^{-3}$. In contrast, observations taken at the University of New Hampshire Atmospheric Observatory at Thompson Farm (located near Durham, NH) during ICARTT were 3.6 $\mu g\,m^{-3}$ with a standard deviation of 5.1 $\mu g\,m^{-3}$ [*Cottrell et al*., 2008].

Evidence of biomass burning plumes was found during ICARTT. Based on measurements from their particle-into-liquid sampler (PILS) that was coupled with a total organic carbon analyzer, *Sullivan et al*. [2006] reported finding biomass burning plumes at altitudes between 3 and 4 km. This result is similar to the observations made during TCAP, where elevated plumes with enhanced biomass burning aerosol (as measured by miniSPLAT) were sampled.

TARFOX was conducted during July 1996 and included the deployment of a number of research aircraft [*Russell et al*., 1999a]. *Hegg et al*. [1997] reported a median AOD value of 0.36 at a wavelength of 405 nm for an atmospheric slab ranging from near the surface to as high as 3.8 km. In comparison, the AOD at a wavelength of 413.6 nm measured over the depth of the atmospheric column at the TCAP AMF site had a median value of 0.16, and approximately 81% of all values of AOD observed during Phase 1 were less than 0.36. These differences in AOD could be caused by a wide range of factors ranging from different transport patterns, geographic dependence, and reductions in emissions between 1996 and the TCAP study period.

The following section will build on the analyses presented in section 3 and investigate the role of aerosol layers aloft on the observed AOD.

4. Analysis of Aerosol Layers Aloft

To better understand the frequency of occurrence and altitudes of aerosol layers over the study area, a 4 year climatology of aerosol layer altitude was compiled prior to TCAP using data from the Cloud-Aerosol Lidar and Infrared Pathfinder Satellite Observations (CALIPSO) [*Chand et al*., 2008; *Vaughan et al*., 2009]. This analysis utilized satellite data collected in July between 2007 and 2010 over the Atlantic Ocean for the region spanning 40–44°N and 68–72°W (Figure 12)—a much longer study period than is possible using only data from studies such as ICARTT and TARFOX. By comparing the aerosol layer top and thickness (which is also computed from the satellite data), aerosol layers aloft can be identified. Specifically, an aerosol layer is classified as being a layer aloft when its thickness is less than two thirds of the height of the top of the layer. For example, if the top of the layer is determined to be 1 km then the layer thickness would need to be less than 0.6 km for the layer to be defined as aloft. It should be noted that some deep aerosol layers, which may in reality consist of different independent aerosol layers, may be misidentified as a single layer leading to individual layers as thick as 4 km. Such

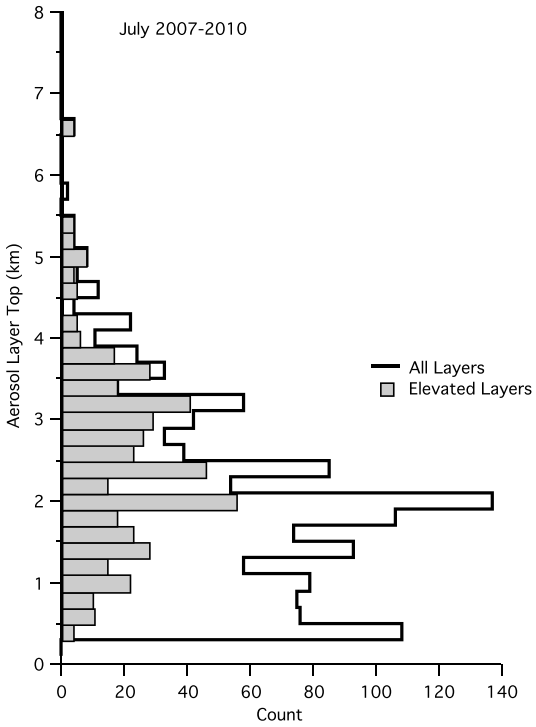

Figure 12. Probability density function of aerosol layer top altitudes derived from the Cloud-Aerosol Lidar and Infrared Pathfinder Satellite Observation (CALIPSO) satellite for July 2007–2010 for all aerosol layers (open) and elevated aerosol layers (filled).

layers, however, account for only a small number of observations and do not change the interpretation of the results. The distribution of the aerosol layer tops derived from the Cloud-Aerosol Lidar with Orthogonal Polarization (CALIOP) is multimodal in the summer. The data (Figure 12) shows one peak near 0.5 km and a second peak near 2 km with a significant number of aerosol layer tops between 2 and 4 km above the surface. Figure 12 shows the distribution of aerosol layer tops for layers aloft (filled bars) and shows that nearly all of the aerosol layer tops observed between 1.5 and 5 km are associated with layers aloft during July.

The airborne HSRL-2 backscatter data show an aerosol layer aloft between 3 to 6 km agl (Figure 6) that is advected into the Cape Cod column on 17 July 2012. The passage of this layer is consistent with the change in AOD observed at the AMF site at the base of the Cape Cod column using the NOAA-MFRSR (Figure S3). These conditions of rapidly changing AOD were not unique during Phase 1. As pointed out by *Kassianov et al*. [2013], there were a number of days during Phase 1 in which the AOD measured at the AMF site changed significantly throughout the day, which had a large impact on the direct aerosol radiative forcing observed at the surface site.

The HSRL-2 is able to measure the aerosol extinction as a function of height, and the contribution of individual layers of the atmosphere to the columnar AOD at 532 nm can be determined by integrating over the layers of interest. Figure 13 shows the fractional contribution to AOD from aerosol above and below 2.64 km. This is obtained by normalizing the fraction of column AOD in each 150 m altitude range for each lidar profile by the total column AOD to remove the impact of horizontal or day-to-day variability in the representation (i.e., the lidar extinction "curtain" has been divided by column AOD on a profile-by-profile basis to preserve information on vertical variability). The fractional contribution is then integrated for the upper and lower portion of the column separately. The split at 2.64 km is chosen with reference to Figure 6a, which shows a local minimum in the aerosol backscatter that lies between the residual layer and the aerosol layer aloft. The contribution to the AOD from both layers (from the surface to 2.64 km and from 2.64 km to the highest altitudes seen by the HSRL-2, approximately 8 km) can be compared. In the maritime column on 17 July nearly all of the AOD is associated with aerosol below an altitude of 2.64 km (Figure 13a). That is not the case within the Cape Cod column, where the AOD associated with the aerosol layer aloft represents as much as 40% of the total AOD within the column.

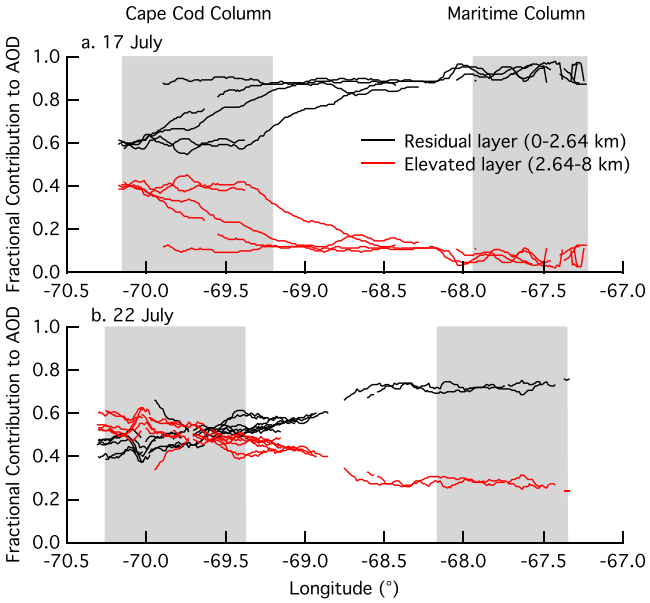

Figure 13. Fractional contribution to column AOD by the layer from the surface to a height of 2.64 km (black) and by the layer from 2.64 km to the top of the HSRL-2 data (red) on (a) 17 and (b) 22 July 2012.

In contrast to the conditions on 17 July, 22 July was marked by much smaller aerosol loading (Figure 5) and aerosol backscatter (Figure 6) in both columns. The columnar AOD measured by the MFRSR at the surface site is nearly constant throughout the day. The residual layer is less well mixed than was found on 17 July and some aerosol layers are evident within and above the residual layer, with the predominant ones occurring between 0 to 2.4 km and 2.9 to 5 km (Figure 6). The G-1 flight pattern intersected both of these layers in each of the columns. Similar to the analysis presented for 17 July, the HSRL-2 measurements of extinction coefficient were integrated over individual layers to yield the contribution of aerosol in each layer to the column AOD (Figure 13b), and, by chance, an altitude of 2.64 km was applicable as a discriminator of the residual and layers aloft in this case as well. Both layers make a significant contribution to the column AOD, with the layer above 2.64 km contributing up to as much as 60% of the column AOD. As that layer becomes geometrically thinner on the eastern edge of the flight pattern, the contribution is reduced somewhat, but it still contributes approximately 30% of the column AOD on both days.

While the preceding analysis is focused on results from 2 days, data from all six cloud-free days sampled during TCAP Phase 1 were also analyzed. On each day, the depth of the residual layer was determined visually using a combination of data from the HSRL-2 and radiosondes. The contribution to the AOD from each HSRL-2 range gate was computed using the same methods applied on 17 and 22 July. Based on this analysis the presence of aerosol layers aloft that contribute 20% or more to the total AOD were observed on 4 of 6 clear days sampled during Phase 1 (Figure 14). On a number of days, the contribution to the AOD from layers above the residual layer contributed nearly 60% of the AOD. There are also periods on 25 July when the layers aloft contribute more than 80% of the AOD, but this particular result should be viewed with caution because of the relatively small AOD observed on that day.

The contribution of the layers aloft to the AOD was found to be a function of distance from shore (Figure 14). On 17, 22, and 25 July the contribution to the AOD from the aerosol layers aloft ranged between 40 and 60% over the AMF site, while further offshore the contribution was much smaller (between 0 and 30%). As discussed previously, the change on 17 July is due to an aerosol layer aloft advecting over the site. The 22 July has a number of persistent layers, but the layer aloft thins with distance from the coast. Conditions are different on 25 July, where the aerosol loading and extinction in the residual layer is relatively small, particularly in the eastern half of the flight pattern, leading to relatively large contributions from the aerosol above the residual layer. Conditions on 21 July were unique, with a relatively large contribution to the AOD from the layers aloft that was nearly constant with distance from the coast. These results regarding the spatial distribution of the AOD should be viewed with some caution, and it should not be assumed that the AOD

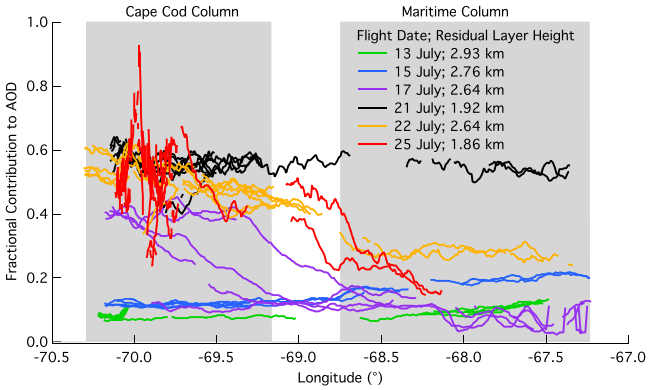

Figure 14. Fractional contribution to the total AOD associated with elevated layers derived from the HSRL-2 data for six clear-sky days as indicated in the legend. Heights shown in the legend are the top of the residual layer obtained from the HSRL-2 data and in situ thermodynamic profiles.

associated with layers aloft is always larger near the coast, rather that there can be large spatial gradients of AOD near the coast of North America that need to be accounted for to accurately simulate the role of aerosol in the climate system.

5. Discussion of Future Opportunities

The results presented in section 3 are focused on only a small part of the data collected during Phase 1 of TCAP, but they serve to highlight how the multiplatform data set can be used to better understand the radiative impact of aerosol, including relationships between the aerosol optical properties, mass loading, and chemical composition. Subsequent papers are planned that will describe Phase 2 (winter time) measurements in more detail, as well as documenting the seasonal cycle of the aerosol and cloud properties near Cape Cod, MA. We also anticipate the data set is well suited to address a wide variety of climate investigations related to both cloud and aerosol of interest to the climate science community; specific examples of some of these uses are briefly described below.

5.1. New Observations From Scanning Cloud Radars

In a previous study, *Feingold et al*. [2003] used data gathered from a number of instruments at the ARM Southern Great Plains site, including a cloud radar, to document aerosol indirect effect in clouds over the that site. More advanced scanning ARM cloud radars (SACR) [*Bharadwaj et al*., 2011; *Kollias et al*., 2014a] were deployed with the AMF for the first time during TCAP and provide an unprecedented view of the 3-D cloud fields in the vicinity of the AMF site. When coupled with the wide range of cloud and aerosol data collected within the Cape Cod column, TCAP will provide a useful data set for further investigations of cloud-aerosol interactions as well as evaluation of cloud statistics derived from large-scale models. Details of the scan strategies and data processing can be found in *Kollias et al*. [2014a], *Kollias et al*. [2014b], and *Lamer et al*. [2014].

The first example from the SACR is a case (Figure 15, top) with a broken fair-weather cumuli field with bases between 3 and 4 km observed on 27 July 2012 (just after the last G-1 flight). In this case, the SACR is located at zero range and height (first two dimensions), and clouds advect over the radar with time (third dimension). The SACR gridded observations show the microscale (internal cloud structure) and macroscale (e.g., cloud aspect ratio, boundaries, and spacing) of the boundary layer clouds. The second example is the same case as presented by *Lamer et al*. [2014] and shows a vertical cut of the gridded 3-D field for a deck of stratocumulus clouds with a vertical extent of less than 500 m that were observed on 19 November 2012 (Figure 15, bottom). The relatively low observed reflectivity in this stratocumulus cloud layer challenged the SACR's detectability threshold resulting in an apparent gradual reduction of the observed cloud thickness with range. Despite this limitation [*Lamer et al*., 2014], the gridded SACR observations can provide valuable information about cloud structure needed for evaluating both high-resolution simulations and for testing cloud parameterizations.

The SACR is complemented by the vertically pointing W band ARM cloud radar. This radar system has participated in a number of different AMF deployments and can be used to measure the cloud boundaries,

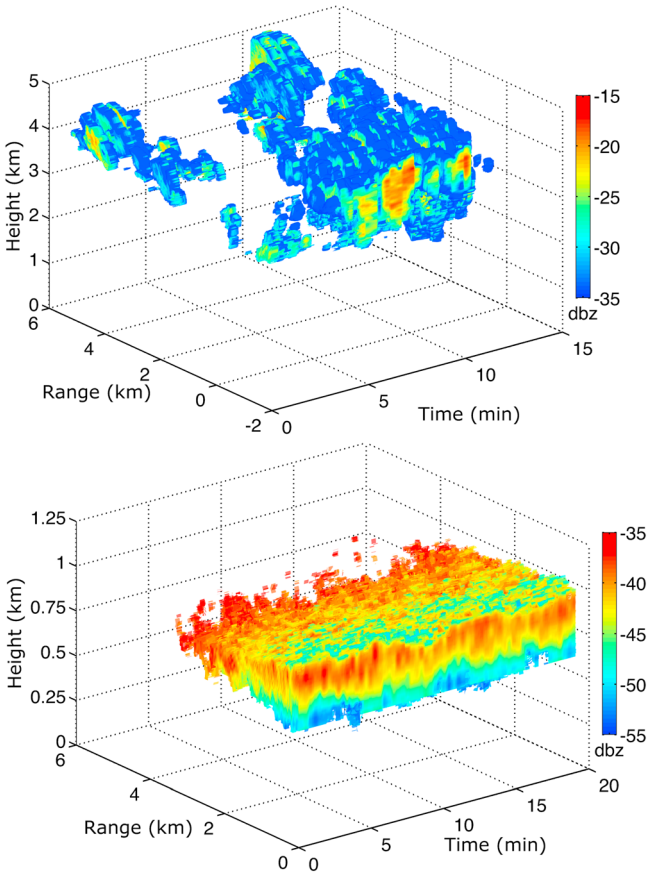

Figure 15. Examples of 3-D gridded radar reflectivity fields from the Ka-band SACR using CW-RHI observations during TCAP. (top) A cumulus field sampled on 27 July 2012 and (bottom) a stratus cloud sampled on 19 November 2012.

cloud microphysical properties, and the strength of updrafts and downdrafts within the cloud. When coupled with the aerosol measurements made at the surface, estimates of the aerosol indirect effects can be made following the work of *Feingold et al*. [2003] that account explicitly for the cloud dynamics and the aerosol loading [e.g., *Berg et al*., 2011]. The scanning Doppler lidar can be used to provide the structure of the subcloud vertical velocity at high temporal and spatial resolution, providing a link between the subcloud and cloud-layer drafts and allowing for the determination of instances in which the clouds are turbulently coupled to the surface.

5.2. Radiative Impacts of Aerosol

Data from TCAP are being used in a wide range of investigations of aerosol and their radiative impacts. Section 4 describes the use of data derived from the HSRL-2 as applied in identifying and characterizing aerosol layers aloft, but new retrievals of key components of the aerosol size distribution are under development [e.g., *Müller et al*., 2014] that can provide detailed information about the aerosol size distribution over significant depths of the atmosphere. The 4STAR is a powerful tool that can be used to determine the AOD and other pollution proxies such as O_3 and NO_2 [*Segal-Rosenheimer et al*., 2014]. Using the TCAP flight plan, the 4STAR can provide the AOD of specific atmospheric layers by comparing values collected at different altitudes [e.g., *Segal-Rosenheimer et al*., 2014; *Shinozuka et al*., 2013]. The miniSPLAT provides a tool to look at the impact of aerosol mixing state on the observed aerosol optical properties.

The surface-based measurements made during TCAP have been used to investigate the impact of diurnal changes in AOD on the radiative forcing [*Kassianov et al*., 2013] and the seasonal variability in the aerosol hygroscopicity, ω_0, and scattering Ånström exponent [*Paluch*, 1979]. A number of optical closure studies that build on the results of *Shinozuka et al*. [2013] and *Volkamer et al*. [2015] are planned that utilize data from both the remote sensing instruments and the surface and airborne in situ measurements (including those related to aerosol

mixing state) made during both Phase 1 and Phase 2 [e.g., *Kassianov et al.*, 2014; *Kassianov et al.*, 2015]. These observations will then be compared to simulations completed using a suite of atmospheric models ranging from particle resolving models to GCMs and will be used to document model performance and suggest improvements that could be made to the parameterizations related to aerosol and aerosol optical properties. For example, within the global Community Atmosphere Model version 5 (CAM5) BC aerosol is assumed to be coated with both sulfate and secondary organic aerosols [*Liu et al.*, 2012], and additional assumptions are made to determine the optical properties of tropospheric aerosol [*Neale et al.*, 2012]. Data from TCAP will be used to evaluate simulations from both WRF-Chem and CAM5 and to test the parameterizations that are routinely applied.

6. Summary and Conclusions

TCAP was a unique yearlong field program designed to investigate a number of important climate related science questions, including those related to aerosol mixing state, aerosol radiative forcing, and cloud-aerosol interactions. TCAP builds on a number of previous field studies through the deployment of new instruments that can provide unprecedented information about details of the aerosol chemical composition and mixing state in conjunction with the aerosol size distributions and optical properties at both the surface, as measured by the U.S. Department of Energy's AMF and aloft using research aircraft.

The analysis of aerosol chemical and optical properties in the Cape Cod and maritime columns highlights the large amount of temporal and spatial variability in the aerosol chemical and optical properties with distance from the coast. Aerosol mass loading varied greatly over the course of the study, with the median value of organic aerosol mass loading varying by a factor of nearly 8 between the days with the greatest and least aerosol loading. The mass fractions of the aerosol also changed, with very small amounts of sulfate containing aerosol in the second half of the study. The median dry ω_0 was found to be greater than 0.92 on all but one flight day, but there was also a decrease in ω_0 during the second half of the study. There were no systematic differences found between the aerosol chemical and optical properties observed in the bottom 400 m of the two columns. In some cases aerosol mass loading was greater in the Cape Cod column, and in other cases the loading was greater in the maritime column, depending on the atmospheric transport patterns as well as other processes such as aerosol aging and formation [e.g., *Knote et al.*, 2014]. The large amounts of temporal and spatial variability in the TCAP data highlight the challenges in accurately simulating the aerosol downwind of North America.

To demonstrate the value of the integrated TCAP data set, two days with very different aerosol loading were selected for detailed analysis of the ω_0, aerosol chemical composition, and aerosol mixing state. Regardless of the mass loading, location, or altitude, the aerosol number fraction was dominated by organics mixed with various amounts of sulfate. The largest variability in the aerosol chemical composition was associated with the loading of rBC, nitrate, aged soot, and biomass burning aerosol. The preliminary results presented here indicate that the ω_0 did not vary significantly with distance from shore, or with the aerosol loading, and was consistent with the observed aerosol mass loading of absorbing and scattering aerosol measured using the combination of a number of instruments, including the SP2, AMS, and miniSPLAT. There were, however, variations in the ω_0 with height, with the smaller observed ω_0 values associated with the lowest altitudes flown by the G-1 (due most likely to ship plumes or other isolated sources), and with aerosol layers aloft (associated with changes in the relatively small amount of rBC and biomass burning aerosol (due most likely to biomass burning over western Canada, western United States, and/or central Canada). Additional analysis is planned to determine if this result is unique to these two days or is consistent throughout the entire study.

One important result from TCAP is the occurrence aerosol layers aloft found above the residual layer during the study period. Aerosol layers aloft particularly those with increased amounts of absorbing aerosol can affect the atmospheric stability by changing the heating profile within the atmospheric column. The layers observed during TCAP occurred on four of six clear-sky research flights, and the layers aloft were found to contribute up to 60% of the total AOD within the atmospheric column. On the 2 days selected for detailed analysis, the chemical composition of the aerosol in the layers aloft had increased amounts of rBC, sulfate, nitrate, and biomass burning aerosol compared to aerosol found within the residual layer. Additional studies will focus on the analysis of regional-scale WRF-Chem and global CAM5 simulations to determine if the aerosol treatments in these models can capture the presence of these layers and their radiative impact.

Acknowledgments

TCAP would not have been possible without the contributions of a large number of individuals, including the G-1 flight crew (M. Hubbell, W. Svancara, J. Hone, and E. Dukes), King Air flight crew (R. Yasky, L. Kagey, M. Wusk, D. Bowser, S. Sims, D. Riddick, and G. Slover), staff from the Cape Cod National Seashore (Superintendent G. Price, L. McKean, C. Skowron, and B. Dougan), Cape Cod National Seashore Atlantic Research and Learning Center, and the radiosonde launch team from the Provincetown Center for Coastal Studies (M. Dunn, S. Greene, C. Hudak, L. Ludwig, J. Melander, D. Minsky, K. Shorr, S. Sollog, D. Towler, E. Larson, D. Dionne, and C. Skowron). The NOAA-MFRSR measurements were supported by NOAA GOES-R Cal/Val Activities within NOAA's National Environmental Satellite, Data, and Information Service. This research was supported by the Office of Science of the U.S. Department of Energy as part of the Atmospheric Radiation Measurement (ARM) and Atmospheric System Research (ASR) programs. RV acknowledges financial support from U.S. DOE award DE-SC0006080. The Pacific Northwest National Laboratory is operated by DOE by the Battelle Memorial Institute under contract DE-A06-76RLO 1830. Data used in this manuscript are available from the ARM data archive (www.archive.arm.gov) or from the corresponding author.

References

Adhikary, B., G. R. Carmichael, Y. Tang, L. R. Leung, Y. Qian, J. J. Schauer, E. A. Stone, V. Ramanathan, and M. V. Ramana (2007), Characterization of the seasonal cycle of south Asian aerosols: A regional-scale modeling analysis, *J. Geophys. Res.*, *112*, D22S22, doi:10.1029/2006JD008143.

Aiken, A. C., P. F. DeCarlo, and J. L. Jimenez (2007), Elemental analysis of organic species with electron ionization high-resolution mass spectrometry, *Anal. Chem.*, *79*(21), 8350–8358, doi:10.1021/ac071150w.

Allan, J. D., et al. (2004), Submicron aerosol composition at Trinidad Head, California, during ITCT 2 K2: Its relationship with gas phase volatile organic carbon and assessment of instrument performance, *J. Geophys. Res.*, *109*, D23S24, doi:10.1029/2003JD004208.

Angevine, W. M., J. E. Hare, C. W. Fairall, D. E. Wolfe, R. J. Hill, W. A. Brewer, and A. B. White (2006), Structure and formation of the highly stable marine boundary layer over the Gulf of Maine, *J. Geophys. Res.*, *111*, D23S22, doi:10.1029/2006JD007465.

Berg, L. K., et al. (2009), Overview of the cumulus humilis aerosol processing study, *Bull. Am. Meteorol. Soc.*, *90*(11), 1653–1667, doi:10.1175/2009bams2760.1.

Berg, L. K., C. M. Berkowitz, J. C. Barnard, G. Senum, and S. R. Springston (2011), Observations of the first aerosol indirect effect in shallow cumuli, *Geophys. Res. Lett.*, *38*, L03809, doi:10.1029/2010GL046047.

Berg, L. K., W. I. Gustafson, E. I. Kassianov, and L. Deng (2013), Evaluation of a modified scheme for shallow convection: Implementation of CuP and Case Studies, *Mon. Weather Rev.*, *141*(1), 134–147, doi:10.1175/mwr-d-12-00136.1.

Berg, L. K., M. Shrivastava, R. C. Easter, J. D. Fast, E. G. Chapman, Y. Liu, and R. A. Ferrare (2015), A new WRF-Chem treatment for studying regional-scale impacts of cloud processes on aerosol and trace gases in parameterized cumuli, *Geosci. Model Dev.*, *8*(2), 409–429, doi:10.5194/gmd-8-409-2015.

Berkowitz, C. M., L. K. Berg, X.-Y. Yu, M. L. Alexander, A. Laskin, R. A. Zaveri, B. T. Jobson, E. Andrews, and J. A. Ogren (2011), The influence of fog and airmass history on aerosol optical, physical and chemical properties at Pt. Reyes National Seashore, *Atmos. Environ.*, *45*(15), 2559–2568, doi:10.1016/j.atmosenv.2011.02.016.

Bharadwaj, N., K. Widener, K. Johnson, S. Collis, and A. Koontz (2011), ARM radar infrastructure for global and regional climate study, in *35th Conference on Radar Meteorology*, Am. Meteorol. Soc., Pittsburgh, Pa.

Blunden, J., and D. S. Arndt (2013), State of the Climate in 2012, *Bull. Am. Meteorol. Soc.*, *94*(8), S1–S258, doi:10.1175/2013BAMSStateoftheClimate.1.

Bond, T. C., and R. W. Bergstrom (2006), Light absorption by carbonaceous particles: An investigative review, *Aerosol Sci. Technol.*, *40*(1), 27–67, doi:10.1080/02786820500421521.

Brioude, J., et al. (2013), The Lagrangian particle dispersion model FLEXPART-WRF version 3.0, *Geosci. Model Dev. Discuss.*, *6*(3), 3615–3654, doi:10.5194/gmdd-6-3615-2013.

Cairns, B. (2003), Polarimetric remote sensing of aerosols paper presented at Geoscience and Remote Sensing Symposium, 2003. IGARSS '03. Proceedings. 2003 IEEE International, 21–25 July.

Chand, D., T. L. Anderson, R. Wood, R. J. Charlson, Y. Hu, Z. Liu, and M. Vaughan (2008), Quantifying above-cloud aerosol using spaceborne lidar for improved understanding of cloudy-sky direct climate forcing, *J. Geophys. Res.*, *113*, D13206, doi:10.1029/2007JD009433.

Chen, F., and J. Dudhia (2001), Coupling an advanced land surface–hydrology model with the Penn State–NCAR MM5 modeling system. Part I: Model implementation and sensitivity, *Mon. Weather Rev.*, *129*(4), 569–585, doi:10.1175/1520-0493(2001)129<0569:caalsh>2.0.co;2.

Clarke, A. D., et al. (2004), Size distributions and mixtures of dust and black carbon aerosol in Asian outflow: Physiochemistry and optical properties, *J. Geophys. Res.*, *109*, D15S09, doi:10.1029/2003JD004378.

Coburn, S., B. Dix, R. Sinreich, and R. Volkamer (2011), The CU ground MAX-DOAS instrument: characterization of RMS noise limitations and first measurements near Pensacola, FL of BrO, IO, and CHOCHO, *Atmos. Meas. Tech.*, *4*(11), 2421–2439, doi:10.5194/amt-4-2421-2011.

Cottrell, L. D., R. J. Griffin, J. L. Jimenez, Q. Zhang, I. Ulbrich, L. D. Ziemba, P. J. Beckman, B. C. Sive, and R. W. Talbot (2008), Submicron particles at Thompson Farm during ICARTT measured using aerosol mass spectrometry, *J. Geophys. Res.*, *113*, D08212, doi:10.1029/2007JD009192.

DeCarlo, P. F., et al. (2006), Field-deployable, high-resolution, time-of-flight aerosol mass spectrometer, *Anal. Chem.*, *78*(24), 8281–8289, doi:10.1021/ac061249n.

Dunagan, S., R. Johnson, J. Zavaleta, P. Russell, B. Schmid, C. Flynn, J. Redemann, Y. Shinozuka, J. Livingston, and M. Segal-Rosenhaimer (2013), Spectrometer for sky-scanning sun-tracking atmospheric research (4STAR): Instrument technology, *Remote Sens.*, *5*(8), 3872–3895.

Earle, M. E., P. S. K. Liu, J. W. Strapp, A. Zelenyuk, D. Imre, G. M. McFarquhar, N. C. Shantz, and W. R. Leaitch (2011), Factors influencing the microphysics and radiative properties of liquid-dominated Arctic clouds: Insight from observations of aerosol and clouds during ISDAC, *J. Geophys. Res.*, *116*, D00T09, doi:10.1029/2011JD015887.

Fehsenfeld, F. C., et al. (2006), International Consortium for Atmospheric Research on Transport and Transformation (ICARTT): North America to Europe—Overview of the 2004 summer field study, *J. Geophys. Res.*, *111*, D23S01, doi:10.1029/2006JD007829.

Feingold, G., W. L. Eberhard, D. E. Veron, and M. Previdi (2003), First measurements of the Twomey indirect effect using ground-based remote sensors, *Geophys. Res. Lett.*, *30*(6), 1287, doi:10.1029/2002GL016633.

Hair, J. W., C. A. Hostetler, A. L. Cook, D. B. Harper, R. A. Ferrare, T. L. Mack, W. Welch, L. R. Izquierdo, and F. E. Hovis (2008), Airborne High Spectral Resolution Lidar for profiling aerosol optical properties, *Appl. Opt.*, *47*(36), 6734–6752.

Hegg, D. A., J. Livingston, P. V. Hobbs, T. Novakov, and P. Russell (1997), Chemical apportionment of aerosol column optical depth off the mid-Atlantic coast of the United States, *J. Geophys. Res.*, *102*(D21), 25,293–25,303, doi:10.1029/97JD02293.

Hignett, P., J. P. Taylor, P. N. Francis, and M. D. Glew (1999), Comparison of observed and modeled direct aerosol forcing during TARFOX, *J. Geophys. Res.*, *104*(D2), 2279–2287, doi:10.1029/98JD02021.

Hobbs, P. V. (1999), An overview of the University of Washington airborne measurements and results from the Tropospheric Aerosol Radiative Forcing Observational Experiment (TARFOX), *J. Geophys. Res.*, *104*(D2), 2233–2238, doi:10.1029/98JD02283.

Janjić, Z. I. (1990), The step-mountain coordinate: Physical package, *Mon. Weather Rev.*, *118*(7), 1429–1443, doi:10.1175/1520-0493(1990)118<1429:tsmcpp>2.0.co;2.

Janjić, Z. I. (2002), Nonsingular implementation of the Mellor-Yamada level 2.5 scheme in the NCEP Meso model *Rep*, 61 pp.

Jayne, J. T., D. C. Leard, X. F. Zhang, P. Davidovits, K. A. Smith, C. E. Kolb, and D. R. Worsnop (2000), Development of an aerosol mass spectrometer for size and composition analysis of submicron particles, *Aerosol Sci. Technol.*, *33*(1–2), 49–70, doi:10.1080/027868200410840.

Jimenez, J. L., et al. (2003), Ambient aerosol sampling using the Aerodyne Aerosol Mass Spectrometer, *J. Geophys. Res.*, *108*(D7), 8425, doi:10.1029/2001JD001213.

Kain, J. S. (2004), The Kain–Fritsch convective parameterization: An update, *J. Appl. Meteorol.*, *43*(1), 170–181, doi:10.1175/1520-0450(2004)043<0170:tkcpau>2.0.co;2.

Kain, J. S., and J. M. Fritsch (1990), A one-dimensional entraining/detraining plume model and its application in convective parameterization, *J. Atmos. Sci.*, *47*(23), 2784–2802, doi:10.1175/1520-0469(1990)047<2784:aodepm>2.0.co;2.

Kassianov, E., J. Barnard, M. Pekour, L. K. Berg, J. Michalsky, K. Lantz, and G. Hodges (2013), Do diurnal aerosol changes affect daily average radiative forcing?, *Geophys. Res. Lett.*, *40*, 3265–3269, doi:10.1002/grl.50567.

Kassianov, E., J. Barnard, M. Pekour, L. K. Berg, J. Shilling, C. Flynn, F. Mei, and A. Jefferson (2014), Simultaneous retrieval of effective refractive index and density from size distribution and light-scattering data: Weakly absorbing aerosol, *Atmos. Meas. Tech.*, *7*(10), 3247–3261, doi:10.5194/amt-7-3247-2014.

Kassianov, E., et al. (2015), Airborne aerosol in situ measurements during TCAP: A closure study of total scattering, *Atmosphere*, *6*(8), 1069–1101.

Knobelspiesse, K., B. Cairns, J. Redemann, R. W. Bergstrom, and A. Stohl (2011), Simultaneous retrieval of aerosol and cloud properties during the MILAGRO field campaign, *Atmos. Chem. Phys.*, *11*(13), 6245–6263, doi:10.5194/acp-11-6245-2011.

Knote, C., et al. (2014), Simulation of semi-explicit mechanisms of SOA formation from glyoxal in aerosol in a 3-D model, *Atmos. Chem. Phys.*, *14*(12), 6213–6239, doi:10.5194/acp-14-6213-2014.

Kollias, P., N. Bharadwaj, K. Widener, I. Jo, and K. Johnson (2014a), Scanning ARM cloud radars. Part I: Operational sampling strategies, *J. Atmos. Oceanic Technol.*, *31*(3), 569–582, doi:10.1175/jtech-d-13-00044.1.

Kollias, P., I. Jo, P. Borque, A. Tatarevic, K. Lamer, N. Bharadwaj, K. Widener, K. Johnson, and E. E. Clothiaux (2014b), Scanning ARM cloud radars —Part II: Data quality control and processing, *J. Atmos. Oceanic Technol.*, *31*, 583–598, doi:10.1175/jtech-d-13-00045.1.

Lack, D., H. Moosmüller, G. McMeeking, R. Chakrabarty, and D. Baumgardner (2014), Characterizing elemental, equivalent black, and refractory black carbon aerosol particles: A review of techniques, their limitations and uncertainties, *Anal. Bioanal. Chem.*, *406*(1), 99–122, doi:10.1007/s00216-013-7402-3.

Lamer, K., A. Tatarevic, I. Jo, and P. Kollias (2014), Evaluation of gridded Scanning ARM Cloud Radar reflectivity observations and vertical Doppler velocity retrievals, *Atmos. Meas. Tech.*, *6*(6), 9579–9621, doi:10.5194/amtd-6-9579-2013.

Li, Z. Q., et al. (2011), East Asian Studies of Tropospheric Aerosols and their Impact on Regional Climate (EAST-AIRC): An overview, *J. Geophys. Res.*, *116*, D00K34, doi:10.1029/2010JD015257.

Liu, X., et al. (2012), Toward a minimal representation of aerosols in climate models: Description and evaluation in the Community Atmosphere Model CAM5, *Geosci. Model Dev.*, *5*(3), 709–739, doi:10.5194/gmd-5-709-2012.

Mather, J. H., and J. W. Voyles (2012), The ARM climate research facility: A review of structure and capabilities, *Bull. Am. Meteorol. Soc.*, *94*, 377–392, doi:10.1175/bams-d-11-00218.1.

Miller, M. A., and A. Slingo (2007), The arm mobile facility and its first international deployment: Measuring radiative flux divergence in West Africa, *Bull. Am. Meteorol. Soc.*, *88*(8), 1229–1244, doi:10.1175/bams-88-8-1229.

Morrison, H., G. Thompson, and V. Tatarskii (2009), Impact of cloud microphysics on the development of trailing stratiform precipitation in a simulated squall line: Comparison of one- and two-moment schemes, *Mon. Weather Rev.*, *137*(3), 991–1007, doi:10.1175/2008mwr2556.1.

Moteki, N., and Y. Kondo (2007), Effects of mixing state on black carbon measurements by laser-induced incandescence, *Aerosol Sci. Technol.*, *41*(4), 398–417, doi:10.1080/02786820701199728.

Müller, D., et al. (2014), Airborne multiwavelength High Spectral Resolution Lidar (HSRL-2) observations during TCAP 2012: Vertical profiles of optical and microphysical properties of a smoke/urban haze plume over the northeastern coast of the US, *Atmos. Meas. Tech. Discuss.*, *7*(2), 1059–1073, doi:10.5194/amtd-7-1059-2014.

Murphy, D. M., D. J. Cziczo, K. D. Froyd, P. K. Hudson, B. M. Matthew, A. M. Middlebrook, R. E. Peltier, A. Sullivan, D. S. Thomson, and R. J. Weber (2006), Single-particle mass spectrometry of tropospheric aerosol particles, *J. Geophys. Res.*, *111*, D23S32, doi:10.1029/2006JD007340.

Myhre, G., et al. (2013), Radiative forcing of the direct aerosol effect from AeroCom Phase II simulations, *Atmos. Chem. Phys.*, *13*(4), 1853–1877, doi:10.5194/acp-13-1853-2013.

Neale, R. B., et al. (2012), Description of the NCAR Community Atmosphere Model (CAM 5.0), *Tech. Note NCAR/TN-486+STR*, Natl. Cent. for Atmos. Res., Boulder, Colo.

Neuman, J. A., et al. (2006), Reactive nitrogen transport and photochemistry in urban plumes over the North Atlantic Ocean, *J. Geophys. Res.*, *111*, D23S54, doi:10.1029/2005JD007010.

Ortega, I., T. Koenig, R. Sinreich, D. Thomson, and R. Volkamer (2015), The CU 2-D-MAX-DOAS instrument—Part 1: Retrieval of 3-D distributions of NO_2 and azimuth-dependent OVOC ratios, *Atmos. Meas. Tech.*, *8*(6), 2371–2395, doi:10.5194/amt-8-2371-2015.

Paluch, I. R. (1979), The entrainment mechanism in Colorado cumuli, *J. Atmos. Sci.*, *36*(12), 2467–2478, doi:10.1175/1520-0469(1979)036<2467:temicc>2.0.co;2.

Quinn, P. K., et al. (2006), Impacts of sources and aging on submicrometer aerosol properties in the marine boundary layer across the Gulf of Maine, *J. Geophys. Res.*, *111*, D23S36, doi:10.1029/2006JD007582.

Redemann, J., R. P. Turco, K. N. Liou, P. V. Hobbs, W. S. Hartley, R. W. Bergstrom, E. V. Browell, and P. B. Russell (2000a), Case studies of the vertical structure of the direct shortwave aerosol radiative forcing during TARFOX, *J. Geophys. Res.*, *105*(D8), 9971–9979, doi:10.1029/1999JD901042.

Redemann, J., et al. (2000b), Retrieving the vertical structure of the effective aerosol complex index of refraction from a combination of aerosol in situ and remote sensing measurements during TARFOX, *J. Geophys. Res.*, *105*(D8), 9949–9970, doi:10.1029/1999JD901044.

Rogers, R. R., et al. (2009), NASA LaRC airborne high spectral resolution lidar aerosol measurements during MILAGRO: Observations and validation, *Atmos. Chem. Phys.*, *9*(14), 4811–4826, doi:10.5194/acp-9-4811-2009.

Russell, P. B., P. V. Hobbs, and L. L. Stowe (1999a), Aerosol properties and radiative effects in the United States East Coast haze plume: An overview of the Tropospheric Aerosol Radiative Forcing Observational Experiment (TARFOX), *J. Geophys. Res.*, *104*(D2), 2213–2222, doi:10.1029/1998JD200028.

Russell, P. B., J. M. Livingston, P. Hignett, S. Kinne, J. Wong, A. Chien, R. Bergstrom, P. Durkee, and P. V. Hobbs (1999b), Aerosol-induced radiative flux changes off the United States mid-Atlantic coast: Comparison of values calculated from sunphotometer and in situ data with those measured by airborne pyranometer, *J. Geophys. Res.*, *104*(D2), 2289–2307, doi:10.1029/1998JD200025.

Samset, B. H., et al. (2013), Black carbon vertical profiles strongly affect its radiative forcing uncertainty, *Atmos. Chem. Phys.*, *13*(5), 2423–2434, doi:10.5194/acp-13-2423-2013.

Schmid, B., et al. (2014), The DOE ARM Aerial Facility, *Bull. Am. Meteorol. Soc.*, doi:10.1175/bams-d-13-00040.1.

Schulz, M., et al. (2006), Radiative forcing by aerosols as derived from the AeroCom present-day and pre-industrial simulations, *Atmos. Chem. Phys.*, *6*(12), 5225–5246, doi:10.5194/acp-6-5225-2006.

Schwarz, J. P., et al. (2006), Single-particle measurements of midlatitude black carbon and light-scattering aerosols from the boundary layer to the lower stratosphere, *J. Geophys. Res.*, *111*, D16207, doi:10.1029/2006JD007076.

Sedlacek, A. J., E. R. Lewis, L. Kleinman, J. Xu, and Q. Zhang (2012), Determination of and evidence for non-core-shell structure of particles containing black carbon using the Single-Particle Soot Photometer (SP2), *Geophys. Res. Lett.*, *39*, L06802, doi:10.1029/2012GL050905.

Segal-Rosenheimer, M., et al. (2014), Tracking elevated pollution layers with a newly developed hyperspectral Sun/Sky spectrometer (4STAR): Results from the TCAP 2012 and 2013 campaigns, *J. Geophys. Res. Atmos.*, *119*, 2611–2628, doi:10.1002/2013JD020884.

Sheridan, P. J., D. J. Delene, and J. A. Ogren (2001), Four years of continuous surface aerosol measurements from the Department of Energy's Atmospheric Radiation Measurement Program Southern Great Plains Cloud and Radiation Testbed site, *J. Geophys. Res.*, *106*(D18), 20,735–20,747, doi:10.1029/2001JD000785.

Shinozuka, Y., et al. (2013), Hyperspectral aerosol optical depths from TCAP flights, *J. Geophys. Res. Atmos.*, *118*, 1–15, doi:10.1002/2013JD020596.

Skamarock, W. C., J. B. Klemp, J. Dudhia, D. O. Gill, D. M. Barker, M. G. Duda, X.-Y. Huang, W. Wang, and J. G. Powers (2008), A description of the advanced research WRF version 3, *Tech. Note NCAR/TN-475+STR*, Natl. Cent. for Atmos. Res., Boulder, Colo.

Slingo, A., et al. (2008), Overview of observations from the RADAGAST experiment in Niamey, Niger: Meteorology and thermodynamic variables, *J. Geophys. Res.*, *113*, D00E01, doi:10.1029/2008JD009909.

Stull, R. B. (1988), *An Introduction to Boundary Layer Meteorology*, pp. 666, Kluwer Acad., Boston, Fla.

Sullivan, A. P., R. E. Peltier, C. A. Brock, J. A. de Gouw, J. S. Holloway, C. Warneke, A. G. Wollny, and R. J. Weber (2006), Airborne measurements of carbonaceous aerosol soluble in water over northeastern United States: Method development and an investigation into water-soluble organic carbon sources, *J. Geophys. Res.*, *111*, D23S46, doi:10.1029/2006JD007072.

Thalman, R., and R. Volkamer (2010), Inherent calibration of a blue LED-CE-DOAS instrument to measure iodine oxide, glyoxal, methyl glyoxal, nitrogen dioxide, water vapour and aerosol extinction in open cavity mode, *Atmos. Meas. Tech.*, *3*(6), 1797–1814, doi:10.5194/amt-3-1797-2010.

Thalman, R., et al. (2015), Instrument intercomparison of glyoxal, methyl glyoxal and NO2 under simulated atmospheric conditions, *Atmos. Meas. Tech.*, *8*(4), 1835–1862, doi:10.5194/amt-8-1835-2015.

Vaden, T. D., D. Imre, J. Beránek, and A. Zelenyuk (2011a), Extending the capabilities of single particle mass spectrometry: I. Measurements of aerosol number concentration, size distribution, and asphericity, *Aerosol Sci. Technol.*, *45*(1), 113–124, doi:10.1080/02786826.2010.526155.

Vaden, T. D., D. Imre, J. Beránek, and A. Zelenyuk (2011b), Extending the capabilities of single particle mass spectrometry: II. Measurements of aerosol particle density without DMA, *Aerosol Sci. Technol.*, *45*(1), 125–135, doi:10.1080/02786826.2010.526156.

Vaughan, M. A., K. A. Powell, D. M. Winker, C. A. Hostetler, R. E. Kuehn, W. H. Hunt, B. J. Getzewich, S. A. Young, Z. Liu, and M. J. McGill (2009), Fully automated detection of cloud and aerosol layers in the CALIPSO lidar measurements, *J. Atmos. Oceanic Technol.*, *26*(10), 2034–2050, doi:10.1175/2009jtecha1228.1.

Volkamer, R., et al. (2015), Aircraft measurements of BrO, IO, glyoxal, NO2, H2O, O2–O2 and aerosol extinction profiles in the tropics: comparison with aircraft-/ship-based in situ and lidar measurements, *Atmos. Meas. Tech.*, *8*(5), 2121–2148, doi:10.5194/amt-8-2121-2015.

Zaveri, R. A., et al. (2010), Nighttime chemical evolution of aerosol and trace gases in a power plant plume: Implications for secondary organic nitrate and organosulfate aerosol formation, NO3 radical chemistry, and N2O5 heterogeneous hydrolysis, *J. Geophys. Res.*, *115*, D12304, doi:10.1029/2009JD013250.

Zelenyuk, A., J. Yang, E. Choi, and D. Imre (2009), SPLAT II: An aircraft compatible, ultra-sensitive, high precision instrument for in-situ characterization of the size and composition of fine and ultrafine particles, *Aerosol Sci. Technol.*, *43*(5), 411–424, doi:10.1080/02786820802709243.

Zelenyuk, A., D. Imre, M. Earle, R. Easter, A. Korolev, R. Leaitch, P. Liu, A. M. Macdonald, M. Ovchinnikov, and W. Strapp (2010), In situ characterization of cloud condensation nuclei, interstitial, and background particles using the single particle mass spectrometer, SPLAT II, *Anal. Chem.*, *82*(19), 7943–7951, doi:10.1021/Ac1013892.

Zelenyuk, A., D. Imre, J. Wilson, Z. Zhang, J. Wang, and K. Mueller (2015), Airborne Single Particle Mass Spectrometers (SPLAT II & miniSPLAT) and new software for data visualization and analysis in a geo-spatial context, *J. Am. Soc. Mass Spectrom.*, *26*(2), 257–270, doi:10.1007/s13361-014-1043-4.

Zhang, Q., et al. (2007), Ubiquity and dominance of oxygenated species in organic aerosols in anthropogenically-influenced Northern Hemisphere midlatitudes, *Geophys. Res. Lett.*, *34*, L13801, doi:10.1029/2007GL029979.